EXPERIMENTAL STUDY ON KINETIC TO THERMAL ENERGY CONVERSION WITH FLUID AGITATION

by Muhammad Haseeb Javed

A thesis submitted to the School of Graduate Studies in

partial fulfillment of the requirements for the degree of

Master of Engineering

Faculty of Engineering and Applied Science

Memorial University of Newfoundland

May 2021

St. John's, Newfoundland, Canada

Abstract

Modern wind turbines are generally used for electricity generation; however, the final form of energy required by many users is thermal energy. Although electrical energy conversion to thermal energy is a high-efficiency process, the efficiency of electricity generation from wind turbines is usually low. In this thesis, a heat generator with fluid agitation is developed and studied. This heat generator converts kinetic energy (e.g. that from a wind turbine) directly to thermal energy through the process of viscous dissipation; this process is achieved through the agitation of the working fluid inside a container. This heat generator uses an optimized flat blade turbine (FBT) impeller and a fully baffled configuration. An electric motor is used to provide the kinetic energy input to the heat generator. A torque sensor, a tachometer, and thermocouples are used to measure the torque, rotational speed (RPM,) and temperature rise in the fluid, respectively. Using the measured quantities, the efficiency of kinetic energy to sensible heat conversion is calculated. Experiments are conducted at different rotational speeds and for different working fluids: distilled water, ethylene glycol, and their respective nanofluids with Al_2O_3 nanoparticles at different concentrations. The experimental results indicate that the heat generator is up to 90% efficient in converting kinetic energy to thermal energy. The temperature rise rate increases with the rotational speed and larger diameter of the impeller. Furthermore, the addition of nanoparticles improves the thermal properties of the fluid, but it does not significantly affect the energy conversion efficiency or the rate of temperature rise in the fluid. A wind turbine can power this heat generator to provide heat to a house or a commercial building. This innovative renewable energy technology would benefit wind rich remote areas with cold weather.

Acknowledgments

I would like to thank my supervisor Dr. Xili Duan, Associate Professor, Faculty of Engineering and Applied Sciences at the Memorial University of Newfoundland (MUN), for his expert advice, constant support, and never-ending encouragement. It was my honor to work under his supervision.

This project would have been impossible without the Terra Nova Young Innovator Award (to Dr. Duan) and support from the School of Graduate Studies. I especially want to acknowledge the Department of Mechanical Engineering at MUN for providing me with excellent resources to support my research.

I want to thank my family and friends, who were a constant source of support and encouragement. Without them, this journey would have been a difficult one.

List of Symbols

$\boldsymbol{A}$ = Area, m^2

B = Baffle length, m

C = Clearance of impeller from the bottom, m

C_d = Coefficient of drag

c_p = Specific heat, $J/kg \cdot K$

D = Impeller diameter, m

D_T = Tank diameter, m

E_t = Energy generated, $kW \cdot h$

e = Energy per unit mass, W/kg

$\boldsymbol{F}$ = Force, N

Fr = Froude number

g = Gravitational acceleration, m/s^2

h = Latent heat of vaporization, kJ$/kg$

I_t = Initial Investment, $

k = Thermal conductivity, $W/(m \cdot K)$

l_o = Length of larger Eddies, m

l_{EI} = Boundary between Energy containing range and inertial range

l_{DI} = Boundary between Dissipation range and inertial range

l = Blade length, m

l_b = Baffle length, m

M = Mass, Kg

M_t = Maintenance cost, \$

m = Mass, Kg

n = Number of blades

n_b = Number of baffles

N = Rotational speed, rad/s

N_b = Baffle Size Ratio

N_p = Power Number

p = Pitch of blades

P = Power, W

pa = Pressure, Pa

Re = Reynold number

$\boldsymbol{R}_{ij}$ = Reynolds stress, Pa

t = Time, s

T = Temperature, K

$\Delta\mathrm{T}$ = Change in temperature, ΔK

$\vec{\boldsymbol{U}}$ = Velocity Vector, m/s

$U(x,t)$ = Velocity Field, m/s

$\boldsymbol{v}$ = Velocity, m/s

w_b = Width of baffle, m

u = X-velocity components, m/s

v = Y-velocity components, m/s

w = Z-velocity components, m/s

x = X-cartesian Coordinates

y = Y-cartesian Coordinates

z = Z-cartesian Coordinates

Z = Liquid depth, m

Greek Letters

ρ = Density, kg/m^3

∂ = Partial derivative

τ_{ij} = Stress

∇ = Del operator

Φ = Viscous dissipation

ϕ = Volume concentration

μ = Viscosity, $Pa \cdot s$

η = Efficiency

η = Kolmogorov length scale

τ = Torque, $N \cdot m$

ω_{cyc} = Angular velocity, rad/s

Subscripts

wf = Working fluid

cnt = Container

nf = Nanofluid

n = Nanoparticle

b = Base fluid

Table of Content

ABSTRACT .... **II**

ACKNOWLEDGMENTS .... **III**

LIST OF SYMBOLS .... **IV**

GREEK LETTERS VII

SUBSCRIPTS VII

LIST OF FIGURES .... **X**

LIST OF TABLES .... **XII**

CHAPTER 1 INTRODUCTION **1**

1.1. BACKGROUND 1

1.2. RESEARCH OBJECTIVES 2

CHAPTER 2 LITERATURE REVIEW **4**

2.1 INTRODUCTION 4

2.2 TURBULENCE 4

2.3 THEORETICAL AND EXPERIMENTAL WORK ON WIND-POWERED HEAT GENERATOR 11

2.4 NANOFLUIDS 12

CHAPTER 3 METHODOLOGY **24**

3.1 INTRODUCTION 24

3.2 DESIGN AND FABRICATION OF HEAT GENERATOR 24

3.3 EXPERIMENTAL SETUP 33

3.4 DESIGN OF EXPERIMENT TECHNIQUE 34

3.5 EXPERIMENTAL APPARATUS 35

3. WORKING FLUID PREPARATION 41

3. EXPERIMENTAL MATRIX 42

3. SUMMARY 44

CHAPTER 4 EXPERIMENTAL RESULTS AND ANALYSIS 46

4.1 INTRODUCTION 46

4.2 SIGNAL FILTERING OF TORQUE DATA 46

4.3 DIFFERENTIAL SCANNING CALORIMETRY (DSC) MEASUREMENTS 49

4.4 THERMAL CONDUCTIVITY AND VISCOSITY 51

4.5 TEMPERATURE MEASUREMENTS 52

4.6 EFFICIENCY OF THE HEAT GENERATOR 60

4.7 TORQUE VALUES 63

4.8 ECONOMIC ANALYSIS 65

4. SUMMARY 67

CHAPTER 5 CONCLUSION AND RECOMMENDATION 69

5.1 CONCLUSION 69

5.2 RECOMMENDATIONS 70

REFERENCES 71

APPENDIX I: ENGINEERING DRAWINGS 84

APPENDIX II: UNCERTAINTY ANALYSIS 87

List of Figures

Figure 2-1: Log scale graph of different length scales and ranges of Eddies. 10

Figure 2-2: Energy Cascade over different regions. 10

Figure 2-3: Increase in Viscosity for different nanofluids versus volume concentration. 16

Figure 3-1: Axial flow type (left) and Radial flow type (right) impellers. 26

Figure 3-2:Power Number vs Reynolds number 29

Figure 3-3: Impellers used in the experimental study. 32

Figure 3-4: a) Experimental Apparatus Pictures. b) CAD Model of Experimental Apparatus. ... 33

Figure 3-5: Schematics of Experimental Setup. 34

Figure 4-1: a) Raw signal in time domain, b) Raw signal in Frequency domain, c) Filtered signal in time domain. 48

Figure 4-2: DSC results for water based nanofluids 50

Figure 4-3: DSC results for EG based nanofluids. 51

Figure 4-4: Al2O3-Water nanofluid temperature increase at 750 RPM. 53

Figure 4-5: Al2O3-Water nanofluid temperature increase at 1000 RPM. 54

Figure 4-6: Al2O3-EG nanofluid temperature increase at 750 RPM. 55

Figure 4-7: Al2O3-EG nanofluid temperature increase at 1000 RPM. 56

Figure 4-8: Water, EG, and Water-EG mixture’s temperature increase at 750 RPM. 57

Figure 4-9: Water, EG, and Water-EG mixture’s temperature increase at 1000 RPM. 58

Figure 4-10: Impeller 1 vs Impeller 2 temperature increase at 750 RPM. 59

Figure 4-11: Impeller 1 vs Impeller 2 temperature increase at 1000 RPM. 59

Figure 4-12: Temperature rise after 60 minutes of fluid agitation.. 60

Figure 4-13: Percentage Efficiency of energy conversion.. 62

Figure 4-14: Torque Value.. 64

List of Tables

Table 1: The summary of experimental results on turbulent flow. 7

Table 2: Price comparison for Nanoparticles. 21

Table 3: Price comparison for Al2O3 nanoparticles 22

Table 4: Price comparison for $Al2O3$ nanofluid 22

Table 5: Measurement uncertainties 41

Table 6: Outline of the experiments under different volume concentrations of nanofluid and impeller RPM values.. 43

Table 7:Mass of $Al2O3$ Nanoparticle needed to make 5 liters of required Volume Concentration of nanofluid. 44

Table 8: Specific Heat values for base fluids 57

Table 9: Cost of Wind Powered Heat Generator System 66

Table 10: LCOE Analysis 68

Chapter 1 Introduction

1.1.Background

The world energy consumption is growing at the highest rate in history, and with the recent shunning of non-renewable energy resources, the majority of this new energy demand is met by renewable energy resources [1]. Wind and solar energy are the most popular source of renewable energy that have attracted most of the investment and research in recent decades. In particular, modern wind turbines are used for electricity generation; however, the final form of energy required by the users in cold regions is thermal energy [2]. For example, an average household in Canada uses 80% of their total energy consumption for heating purposes [3]. Although electrical energy conversion to thermal energy is a high-efficiency process, electricity generation efficiency from wind turbines is usually low, which pushes down the process's overall efficiency. The efficiency of electricity generation from wind is around 35% [104].

This thesis proposes a novel heat generator that converts the kinetic energy from wind directly into thermal energy through agitation of a working fluid in a cylindrical container; this process is known as viscous dissipation. The concept of heat generation using viscous dissipation is nothing new James Prescott Joule used the same process to prove the conversion of mechanical work into heat, leading to the development of the first law of thermodynamics [4].

This heat generator can be powered by a wind turbine and can be deployed in any cold region with an abundance of wind flow. For Canada, particularly the northern communities, coastal regions, and remote islands can be primary customers. According to some estimates, 60 GW of power can be harnessed from onshore wind energy in Newfoundland alone [5].

According to the Remote Communities Energy Database, about 250 remote communities and 185,000 people in Canada are not connected to North American electricity grid; about 87 percent of electricity is generated using non-renewable resources in these communities [6] along with 98 percent of heating [7].

The innovative renewable energy technology proposed in this study would benefit economic prosperity, environmental sustainability, and social well-being for many regions in the world.

1.2. Research Objectives

This thesis focuses on the heat generator design; experimental studies are conducted on the heat generator to determine the temperature rise due to fluid agitation. The objectives of this research include the following:

- The effects of impeller diameter, rotational speed, and working fluid properties on the rate of temperature rise in the fluid.
- The conversion efficiency of kinetic energy into sensible heat energy.
- Impact of nanoparticle addition on device performance.
- Effects of nanoparticle concentration on specific heat of the nanofluids.
- The temperature rises characteristics due to changing viscosity and specific heat of the working fluids.

1.3 Structure of the Thesis

Chapter 2 covers the fundamental fluid mechanics concept of turbulence and discuss previous similar research in the field. While there was no experimental research directly related to heat generator using nanofluids, similar projects explored the temperature rise due to fluid agitation. In addition to this, chapter 2 covers the nanofluid characteristics and impact of nanoparticle addition on the base fluid thermal fluid properties.

Chapter 3 covers the experimental technique design and the selection of the best method for the study. The design and fabrication of the heat generator prototype is discussed. In addition to this, chapter 3 also discusses the preparation of nanofluids and the experimental procedure.

Chapter 4 presents the experimental data from the temperature rise study and differential scanning calorimetry (DSC) study. The data is analyzed according to the research objectives, and important variables in the performance of device are identified.

Chapter 5 presents the conclusions from the thesis and provides suggestions for further studies on the topic.

Chapter 2 Literature Review

2.1 Introduction

Chapter 2 contains a short introduction on governing equations of viscous dissipation, a general discussion on the turbulence phenomena, and a discussion on factors that impact viscous dissipation. This chapter also looks at previous attempts to harness viscous dissipation and details some similar projects. Literature is also explored to identify the nanofluid that is both economical and has superior thermal fluid properties.

2.2 Turbulence

Turbulence is the unsteady violent motion of a fluid, a readily observable natural phenomenon, the smoke coming out of house chimney to mixing sugar in a hot coffee cup are all examples of turbulent flow. The heat generator prototype will rely on the turbulence phenomenon to generate heat, which is why an understanding of turbulence is needed.

Turbulent flow is an unsteady, irregular, random, chaotic, and seemingly unpredictable flow of fluid. The turbulent flow velocity field varies significantly where a velocity field is defined as $U(x, t)$, where x is the location, and t is the time. The turbulent motion is random and irregular in both time and space. A defining feature of turbulent flow is the ability to transport and mix the fluid momentum more effectively than a laminar flow.

Turbulent motion occurs at a high Reynolds number, and at a high enough Reynolds number, one can observe "a separation of scale" [6]. The large-scale motion in a turbulent flow is a function of geometry (e.g., boundary conditions influence the scale), while the small-scale motion in the turbulent motion is only a function of viscosity and the rate at which energy is received from large scales. In other words, the small-scale motion of turbulent flow has a universal form, which is the same for every flow independent of the geometry.

The Navier-Stokes equations are remarkable because a set of seemingly simple equations can completely define a flow field, but unfortunately, this feature does not mean that it can be solved easily. While the Navier-Stokes equations can be solved for flows at low Reynolds numbers using direct numerical simulation (DNS), it is not possible to solve the equation for turbulent flows at higher Reynolds numbers. In turbulent flows, the Navier-Stokes equations become almost impossible to solve because of the unsteady nature of flow. Navier-Stokes equations describe every time scale and every detail of the velocity field; this does not help because the velocity field is random and chaotic. Hence even though the Navier-Stokes equations are accurate, they are not directly solvable for turbulent flows.

The unsteady nature of turbulent flow is because of perturbations in initial and boundary conditions of any turbulent flow; these perturbations include roughness of the surface, the vibration of the setup, presence of impurities, and the difference in fluid properties due to small temperature differences. Although these perturbations exist in laminar flow, the defining feature of turbulent flow is its sensitivity to these perturbations.

The difficulty to define a turbulent flow is overcome by defining the equations in terms of a mean velocity field instead of a velocity function; the mean velocity field varies smoothly with time and space. A model based on such statistics leads to a version of the Navier-Stokes equation that is tractable as can be seen in equations (1)-(2).

Continuity Equation:

$$\frac{\partial \rho}{\partial t}\ \nabla.\left(\rho\vec{\boldsymbol{U}}\right)\ = 0 \qquad (1)$$

Momentum Equation:

$$\rho\frac{\partial \vec{\boldsymbol{U}}}{\partial t} = \rho\vec{g} - \nabla \mathrm{p} + \nabla.\tau_{ij} \qquad (2)$$

Energy Equation:

$$\rho\frac{\partial e}{\partial t} + p\left(\nabla.\vec{\boldsymbol{U}}\right) = \nabla.(k\nabla \mathrm{T}) + \Phi \qquad (3)$$

$$\rho\frac{\partial e}{\partial t} + p\left(\nabla.\vec{\boldsymbol{U}}\right) = \nabla.(k\nabla \mathrm{T}) + \Phi$$

The Φ term in equation (3) denotes the viscous dissipation term in the energy equation, and for a three-dimensional flow in the cartesian coordinates system, the dissipation term is presented in equation (4). The first feature of the equation is that viscous dissipation is proportional to the fluid viscosity, which means that as the liquid viscosity increases, so does the viscous dissipation.

$$\Phi = \upsilon\left(2\left(\frac{\partial u}{\partial x}\right)^2 + \left(\frac{\partial v}{\partial x}\right)^2 + \left(\frac{\partial w}{\partial x}\right)^2 + \left(\frac{\partial u}{\partial y}\right)^2 + 2\left(\frac{\partial v}{\partial y}\right)^2 + \left(\frac{\partial w}{\partial y}\right)^2 + \left(\frac{\partial u}{\partial z}\right)^2 + \left(\frac{\partial v}{\partial z}\right)^2 + 2\left(\frac{\partial w}{\partial z}\right)^2 + 2\left(\frac{\partial u}{\partial y}\right)\left(\frac{\partial v}{\partial x}\right) + 2\left(\frac{\partial u}{\partial z}\right)\left(\frac{\partial w}{\partial x}\right) + 2\left(\frac{\partial v}{\partial z}\right)\left(\frac{\partial w}{\partial y}\right)\right) \qquad (4)$$

There are 12 terms in the dissipation part of the energy equation, making it nearly impossible to do any meaningful theoretical analysis on the equation**.** One approach early researchers used was to assume local isotropy of the fluid flow. This would mean that the first nine terms are the same in magnitude, and the last three are half in magnitude compared to the other terms [7]. While this approach is simple to implement, several researchers found that flow is seldom isotropic; hence the assumption is unfound [8-11]. The summary of the results from Laufer experiments are presented below in Table 1 [12]. For a fully isotropic flow, all the fraction values between different terms should be equal to 1, but as it can be seen from the table, the value fluctuates and is rarely near the value 1.

Table 1: The summary of experimental results on turbulent flow. [12]

Experiment Detail	**Reynolds number**	$\frac{2\left(\frac{\partial u}{\partial x}\right)^2}{\left(\frac{\partial v}{\partial x}\right)^2}$	$\frac{2\left(\frac{\partial u}{\partial x}\right)^2}{\left(\frac{\partial w}{\partial x}\right)^2}$	$\frac{2\left(\frac{\partial u}{\partial x}\right)^2}{\left(\frac{\partial u}{\partial y}\right)^2}$	$\frac{2\left(\frac{\partial u}{\partial x}\right)^2}{\left(\frac{\partial u}{\partial z}\right)^2}$
Pipe flow near wall	50,000	3.3	1.8	0.40	0.40
Pipe flow near half radius	50,000	1.0	0.83	0.69	0.56
Pipe flow near wall	500,000	1.73	1.73	0.93	0.93
Pipe flow near half radius	500,000	1.40	1.12	0.80	0.80

Some of the terms from viscous dissipation term are easy to measure experimentally; for example, the terms $\left(\frac{\partial u}{\partial x}\right)^2$ can easily be measured using a single hot wire while $\left(\frac{\partial v}{\partial x}\right)^2, \left(\frac{\partial w}{\partial x}\right)^2$ can be measured using an X wire, Taylor's hypothesis can be used to derive these quantities from temporal derivatives of u, v, w [7]. The $\left(\frac{\partial u}{\partial y}\right)^2$ and $\left(\frac{\partial u}{\partial z}\right)^2$ terms could be measured using two parallel hot wires; this is why multiple published values for these terms are available in the literature. But for the remaining terms like $\left(\frac{\partial v}{\partial y}\right)^2$, $\left(\frac{\partial w}{\partial y}\right)^2$, $\left(\frac{\partial v}{\partial z}\right)^2$, $\left(\frac{\partial w}{\partial z}\right)^2$, $\left(\frac{\partial u}{\partial y}\right)\left(\frac{\partial v}{\partial x}\right)$, $\left(\frac{\partial u}{\partial z}\right)\left(\frac{\partial w}{\partial x}\right)$ it is not easy to measure their value as two X-wires need to be placed very close, which is difficult to implement in a lab. On the other hand, the term $\left(\frac{\partial v}{\partial z}\right)\left(\frac{\partial w}{\partial y}\right)$ is nearly impossible to measure with any reasonable accuracy because it requires four X-wires [7].

2.2.1 Reynolds Stresses

The Reynolds Average Navier-Stokes (RANS) equation can be split into average and fluctuating parts using the statistical methods. This technique introduces a new stress term in the equation with the form of $\rho\overline{u_i'u_j'}$, this term is usually known as Reynolds Stress and can be written as $\boldsymbol{R}_{ij}$.

If $\overline{u_i'u_j'}$ term was zero, the N-S equation for the velocity field and the average velocity field would be identical, so it becomes clear that Reynolds stress plays a defining role in modeling the turbulent flow. These Reynold stresses originate from the momentum transfer by the fluctuation in the velocity field.

There are four independent equations for a three-dimensional flow, e.g., continuity equation and three momentum equations that solve for four unknown quantities but in case of the RANS equation; there is an extra unknown, Reynolds stress. This presents a closure problem; hence the Reynold equations cannot be solved unless there is some information about the Reynolds stress, and this is where turbulence modeling comes into play. $k - \omega$, $k - \epsilon,\ SST$ (Shear Stress Transport) are standard models used in Computational Fluid Dynamics (CFD) to solve this closure problem. Due to this study's scope, CFD modeling is not attempted, and the phenomena is studied experimentally.

2.2.2 Scales of Turbulent Motion

Visual inspection of a turbulent flow will clearly show that motion in the flow varies in size. There are eddies the size of the vessel diameter; simultaneously, the smaller eddies are hardly visible to the naked eye. In a turbulent flow, energy enters through a production mechanism (e.g., impeller stirring the fluid in this study), and this is the largest scale of motion; this energy is progressively transferred to smaller scales until it reaches the smallest scale and dissipated by viscous action [13]. The smallest scales were identified by Kolmogorov, which now bears his name [14].

Eddies do not have a strict definition. Instead, they are loosely defined as turbulent motion that is coherent over the region of size l. The largest eddies consist of the length scale, which is comparable to the size of the domain. These larger eddies are unstable in nature and break up into smaller and smaller eddies; this process of eddy breakup continues until the local Reynold number becomes sufficiently small, and eddy motion becomes stable [6]. Figure 2-1 shows the three separate ranges and their comparable scales. At a smaller local Reynolds number, the viscosity is dominant, and this is where most of the dissipation occurs. In homogenous turbulence the dissipation rate is dependent on the introduction of energy into the system, and it is interesting to note that both of these quantities are equal. Kolmogorov argued that the smallest eddies are statistically isotropic; this implies that the directional information of fluid is lost in the scale reduction.

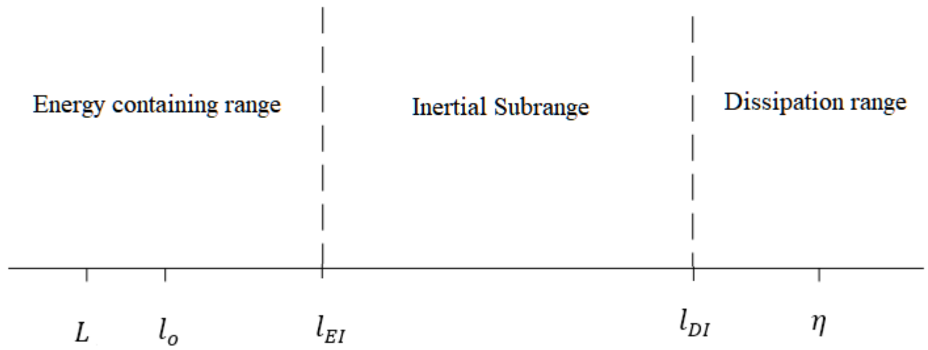

Figure 2-1: Log scale graph of different length scales and ranges of Eddies.

Figure 2-2 details the energy transfer over the different regions. It can be seen that the energy transfers from left to the right, with the largest eddies of the size l_o on the left-hand side. The energy containing range has the highest amount of turbulent energy. The viscous effect and viscous dissipation are minimal in the inertial subrange as inertial effects are dominant. Nearly all dissipation takes place in the dissipation range. The length l_{EI}, l_{DI} define the boundary between regions, E here stands for energy-containing range, I stands for inertial range, and D stands for dissipation range. L is characteristic length, and η is the Kolmogorov length scale.

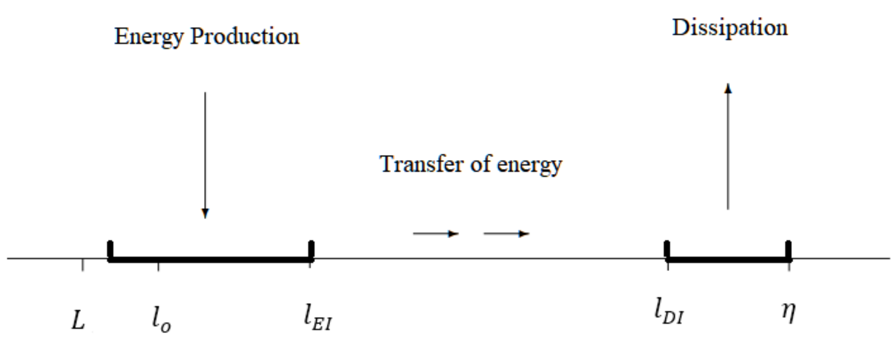

Figure 2-2: Energy Cascade over different regions.

As mentioned above, the dissipation rate and the total amount of dissipation energy depend on the rate and amount of energy introduced into the system [6]. This represents the fact that no energy is stored during the energy cascade process. For the experimental study, this signifies that all the kinetic energy that goes into the vessel will be converted entirely into thermal energy.

2.3 Theoretical and Experimental work on Wind-Powered Heat Generator

The concept of direct conversion of kinetic energy into thermal energy using nanofluids as working fluid is entirely novel, so there is no work on this topic. However, there are similar projects which tried to harness the heat generated from the viscous dissipation.

Multiple researchers [15-17] have attempted to model the wind-powered heat generator system theoretically under idealized conditions, like a hundred percent conversion of mechanical work into heat energy. Unfortunately, these studies are not backed by any experimental results. In fact, a few papers only focused on optimizing the torque-speed characteristics of the wind turbine [15-16] and did not address the mechanism behind heat generation. A paper discussed harnessing the heat from viscous dissipation to power a maritime distiller [17], but again this study looked at the problem theoretically and did not validate with any experimental data to back up the claim.

The closest attempt at the wind to thermal conversion in the literature is an experimental study by researchers at Northwest A&F University in Shaanxi, China [18]. This study investigated the temperature rise and percentage efficiency of such a system for three different base fluids. While this study concluded the viability of such a concept, the percentage conversion of kinetic to thermal energy was relatively low and not what theoretical analysis would conclude.

Another experiment conducted by chemical engineering researchers at IIT-Delhi investigated impeller design characteristics using temperature rise data from their experiments [19]. While the experimental setup was not designed to generate viscous dissipation(heat), and the heat was just a byproduct of the stirring action, the vessel design is similar to the proposed heat generator design. Additionally, the results from this study corroborate with theoretical analysis results.

A conference paper published in 2013 provides us with valuable experimental data on the temperature rise due to mechanical work [20]. This paper theorized a "cavitation heat pump" which could heat the liquid for use at home. The authors assumed that the cavitation process provided heat and missed the viscous dissipation phenomena entirely, but their data is still valuable proof of the concept.

2.4 Nanofluids

A nanofluid is a fluid that contains colloidally suspended solid particles of size between 1nm to 100nm in an organic or inorganic base fluid. Ever since Choi's innovative work on nanofluids in 1995 [21] the interest of research community has been kindled into the amazing thermal fluid property of nanofluids. A nanofluid is observed to have better heat transfer properties compared to the base fluid [22] and is considered as a "new generation of heat transfer fluids."

Because of the small size of nanoparticles, the nanofluids act like a single-phase fluid instead of a two-phase mixture [23], this gives nanofluids numerous advantages compared to the two-phase mixtures of microparticles. The microparticle mixtures are found to have sedimentation, which leads to clogging and erosion of pipes and offers poor stability. Nanofluids on the other hand largely reduce concerns about sedimentation, clogging, and erosion along with providing additional benefit of offering more stability. [23].

An essential requirement from nanofluid is durability, stability, and even suspension of nanoparticles in the fluid. Furthermore, the addition of nanoparticles should not bring about any chemical change in the fluid. There are multiple examples of nonmetallic nanoparticles and metallic nanoparticles that could be used to prepare nanofluids. [23] Some popular base fluids are water, ethylene glycol (EG), transformer oil, and mineral oil.

While the thermophysical properties of all the major fluids used in engineering are well documented in handbooks and literature, the same cannot be said about nanofluids. The literature available on nanofluids is incomplete and has significant gaps. In the following section, experimental results and models related to nanofluids are discussed to better understand nanofluids' properties and, consequently, select a nanofluid for the experiments that is both optimized for good performance and economical. Nanofluid has to be economical to be used in future commercialization of the novel heat generator.

2.4.1 Preparation of Nanofluids.

There are various methods to produce a nanofluid, and all these methods can be classified as single-step and two-step methods. [22] In the single-step method, the nanoparticle is produced and dispersed in the base fluid simultaneously, which avoids the agglomeration of nanoparticles, but a side effect is that residue of reaction is left behind, affecting nanofluids' purity [25]. This method is not economical, and large batches are hard to produce.

In the two-step method nanoparticles are produced as a dry powder using chemical vapor deposition processes, and later this powder is dispersed in the base fluid using mechanical stirring, ultrasonic mixing, electromagnetic agitation, and homogenizing. The two-step method is used for the commercial production of nanoparticles. The most significant disadvantage of this method is the agglomeration of nanoparticles which leads to lower nanofluid stability.

While there are many ways to access nanofluid stability like Zeta Potential Analysis and

Spectral Absorbency Analysis, the simplest way is the sedimentation process where the fluid is left stationary and any sediments formed can be visually inspected. Stability is an issue in nanofluids that are stationary, but as heat generator will be in continuous motion, stability is not a big issue for this study.

2.4.2 Properties of Nanofluids

The literature on Nanofluids is by no means exhaustive, there is a plethora of experimental data that is used to derive correlations, but it is important to note that these correlations are inconsistent and even contradictory in some matters as discussed later. In this section, general trends in nanofluids' properties are discussed.

2.4.2.1 Density

Nanofluids' density is not widely reported in the literature, but few correlations could be used to calculate nanofluids' density. It is well established that the density of nanoparticles is higher than base fluid, so as the concentration of nanoparticles increases, so does the nanofluid density. Pak and Cho [24] introduced a mixing equation (5) for nanofluid density which is a function of volume concentration.

$$\rho_{nf} = \phi\rho_n + (1-\phi)\rho_b \tag{5}$$

In this equation, ρ is the density, ϕ is the volume concentration, subscript "nf" stands for nanofluid, "n" stands for nanoparticle, and "b" stands for base fluid. Saeedinia et al [25] experimented on CuO-based nanofluid and found that the above relation is quite accurate for low volume concentration but for higher volume concentration, the difference in values increases. In addition to that, the above relation is only valid for temperatures around room temperature as studies have shown that the density of nanofluid is inversely related to an increase in temperature [26-28]. For the experiments, the density value can be easily calculated using the volume and weight of nanofluid.

2.4.2.2 Viscosity

Many models try to predict a nanofluid viscosity, but all of these models are limited in their prediction. Albert Einstein formulated the first model for viscosity in 1906; this model predicted effective viscosity as a volume concentration function [29]. This model is extremely limited as it can only predict the viscosity for spherical nanoparticles that are less than 1.0 % in volume concentration.

$$\mu_{nf} = 1 + 2.5\phi \tag{6}$$

Here μ is the viscosity, and ϕ is the volume concentration. Brinkman updated Einstein's model in 1952 to make it more effective at higher concentrations of nanoparticles [30], Batchelor later developed a model to include Brownian random motion in 1977 [31]. Pak and Cho [24] also developed a model that predicts a nanofluid viscosity at room temperature. Brickman, Batchelor, and Pak & Cho models are presented in Equation (7), (8), (9), respectively.

$$\mu_{nf} = \frac{1}{(1-\phi)^{2.5}} \tag{7}$$

$$\mu_{nf} = 1 + 2.5\phi + 6.5\phi^2 \tag{8}$$

$$\mu_{nf} = 1 + 39.11\phi + 533.9\phi^2 \tag{9}$$

Experiments have shown that these models are not very accurate as they are developed for a spherical solid particle, while the nanoparticles are rarely spherical. Additionally, these models do not take any factor apart from volume concentration into account.

In the absence of a reliable model, data from experimental studies can be used to get reliable information about nanofluid viscosity. Multiple experimental studies have shown that increasing the nanoparticle concentration increases the viscosity as well [32-35]. Studies on water and ethylene glycol have shown the same trend that viscosity is proportional to nanoparticle volume concentration [36-37].

It should also be noted that nanofluid viscosity is not just a function of volume concentration but also a function of nanoparticle shape, size, and temperature [38]. From literature, experimental data for SiC, CNT, CuO, Al_2O_3 nanofluids clearly shows that viscosity decrease with the increase in temperature [39-42]. Another study notes that the trend of decreasing viscosity is exponential with increasing temperature for CuO, Al_2O_3 , and $SiO2$ nanofluids. [43].

Figure 2-3 is developed using experimental data from a number of experimental studies. [44-52]. It is interesting to note that the same nanoparticle with different size has varied changes in viscosity.

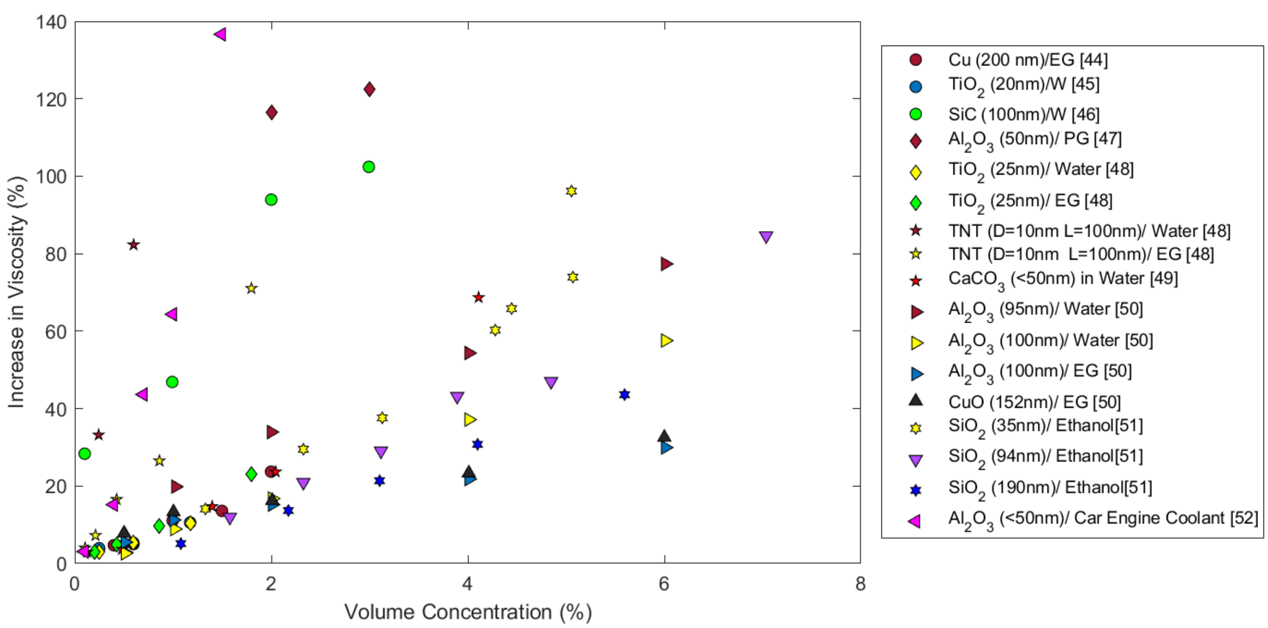

Figure 2-3: Increase in Viscosity for different nanofluids versus volume concentration.

2.4.2.3 Specific Heat Capacity

Specific Heat Capacity is measured as the amount of heat required to raise one unit mass temperature by one Kelvin. This section will look at different nanofluids and the factors that may affect their heat capacity values.

There are many theoretical models to predict the specific heat capacity of nanofluids. One model was developed by Pak and Cho [24] and was based on the mixture of base fluid and nanofluids. It is given below in equation (10).

$$C_{nf} = \phi C_n + (1-\phi) C_b \tag{10}$$

In this equation C is specific heat capacity, ϕ is the volume concentration, the subscript "nf" stands for nanofluid, "n" stands for nanoparticle, and "b" stands for base fluid.

Xuan and Roetzel [53] modified this model by developing a new relation based on the thermal equilibrium between base fluid and nanoparticles. This relation is given below in equation (11).

$$(\rho C)_{nf} = \phi (\rho C)_n + (1-\phi)(\rho C)_b \tag{11}$$

In this equation C is specific heat capacity, ϕ is the volume concentration, ρ is the density, and subscript "nf" stands for nanofluid, "n" stands for nanoparticle, and "b" stands for base fluid. The density of nanofluid ρ_n here is calculated using equation (5).

Zhou et al. [54] noted the equations (10)-(11) are not valid for higher volume concentrations of nanoparticles, so they modified equation (11), and the resulting equation is presented in (12).

$$C_{nf} = \frac{\phi(\rho C)_n + (1-\phi)(\rho C)_b}{\rho_b + (1-\phi)\rho_n} \quad (12)$$

An experimental study by Zhou et al. [54] concluded that equation (12) is more accurate at predicting specific heat capacity values of water-based Al_2O_3 nanofluids at higher volume concentration.

Satti et. al [55] conducted experimental analysis on five nanofluids: $Al_2O_3, ZnO, TiO_2, CuO, and\ SiO_2$ dispersed in 60:40 mixture of propylene glycol and water, they noted that an increase in nanoparticles volume concentration decreases the nanofluid's specific heat. They also noted that for varying sizes of Al_2O_3 nanoparticle, from 15nm to 45 nm, the specific heat was nearly the same, and that particle size does not play a major part. The same observation was true for ZnO nanoparticle, where the particle size was varied from 36nm to 76 nm, and no significant change in specific heat was observed [55].

On the other hand, experimental data indicate that specific heat value increases with an increase in temperature [55] [56]. This contradictory nature of experimental data found in literature makes it even more important to check the specific heat of nanofluids used in this study experimentally.

Specific heat's accurate value is needed to analyze experimental data as it will be used to calculate the increase in sensible heat energy, and consequently, the energy dissipated. For this reason, nanofluid's specific heat is found experimentally using Differential Scanning Calorimeter (DSC) technique, as discussed in section 4.3.

2.4.2.4 Thermal Conductivity

Thermal conductivity is an important property of a nanofluid. It is defined as the rate at which heat is passed through the nanofluid. It is well established that the thermal conductivity for solids is higher than that for liquids; this is partly why solid nanoparticles' addition increases the base fluid's thermal conductivity.

Many correlations have been developed to get a theoretical formula that can determine the thermal conductivity of a nanofluid. The first significant effort was made by Maxwell [57], who came up with a relation (13) to predict the thermal conductivity of spherical micrometer-scale particles in a base fluid. Consequently, this relation is only valid for low concentration, relatively spherical nanoparticles.

$$\frac{k_{nf}}{k_b} = \frac{(k_n + 2k_b) + (2\phi(k_n - k_b))}{(k_n + 2k_b) - (\phi(k_n - k_b))} \tag{13}$$

In this equation, "k" is the thermal conductivity, ϕ is the volume concentration, and "n" subscript is nanoparticle, "b" is base fluid, and "nf" is nanofluid.

Bruggeman [58] modified Maxwell's relation for higher particle concentration; this relation (14) is given below.

$$0 = \phi\left(\frac{k_n - k_{nf}}{k_n - 2k_{nf}}\right) + (1 - \phi)\left(\frac{k_b - k_{nf}}{k_b - 2k_{nf}}\right) \tag{14}$$

The limitation of both Maxwell and Bruggeman's relation is that they were derived for a spherical shape. To overcome this problem, Hamilton and Crosser [59] developed a model (16) that was effective for any particular nanoparticle shape. They achieved this by introducing a parameter "n" in their equation that accounted for the particle shape.

$$\frac{k_{nf}}{k_b} = \frac{(k_n + (n-1)k_b) + (n+1)\phi(k_n - k_b)}{(k_n + (n-1)) - (\phi(k_n - k_b))} \tag{15}$$

All these models effectively predict the thermal conductivity at low temperature and low volume concentration only. One must rely on experimental data to find reliable results for higher concentration and higher temperature situations.

From literature, it is clear that thermal conductivity of nanofluid increases with an increase in volume concentration of nanoparticles; for example, an increase of 26% was reported in a paper for 5% volume concentration of Al_2O_3 at room temperature [60].

The size of a nanoparticle also has a great impact on the thermal conductivity. Smaller nanoparticle will have a higher surface area to volume ratio; thus, it will also have a higher thermal conductivity. A paper by Anoop et al. found that the thermal conductivity of Al_2O_3 nanofluid with an average nanoparticle size of 45nm was higher than nanofluid with 150nm average nanoparticles size [61].

Temperature is another factor for thermal conductivity of a nanofluid, a study for water-based Al_2O_3 and CuO show that temperature increase is directly proportional to thermal conductivity [62]. Thermal conductivity is not directly investigated in this thesis as the heat generator prototype is a closed system with no heat transfer taking place.

2.4.3 Economic Consideration and Nanofluid Selection.

There are many nanoparticles and nanofluid suppliers; while most of these suppliers cater to academia and supply only a smaller amount of nanoparticles, there are a few suppliers that can support industrial operation and provide a bulk supply of nanoparticles if needed. To understand the nanoparticles' pricing, only industrial suppliers were considered as they would be a feasible option for when the heat generator is commercialized.

US Research nanomaterials, Inc was selected for the supply of nanoparticles because of their established reputation and ability to supply an industrial operation. Price comparison for a few of the most investigated nanoparticles is given in table 2. The preliminary calculations state that 400-500 grams of nanoparticles would be needed to make a nanofluid, so the price for 500 grams of the nanoparticle is presented below.

The nanoparticles' prices vary greatly; the single element nanoparticles are the most expensive and are not available in large quantities. From table 2, it can be observed that on the one hand, there is Aluminum Oxide, which costs $115 for half a kilogram, while on the other hand, there is Zn, which costs $559 for half a kilogram.

Aluminum Oxide nanoparticle is the most reasonable choice as it is easy to source, cost on the lower end of the spectrum, and a large amount of literature review data is available for its performance in both water and EG. Aluminum Oxide shows a good improvement in base fluids' viscosity, as shown in figure 2-3. In addition to this Aluminum Oxide nanoparticle is low in toxicity and safe to work within the lab environment.

Table 2: Price comparison for Nanoparticles. [63]

Name	Price for 500 grams / USD
Cu, 90-250nm	450
TiO_2, 30nm	298
SiC, <80nm	399
CuO, 80nm	188
SiO_2, 60-70nm	125
Al_2O_3, 135nm	115
MgO, 100nm	175
Fe_3O_4, 20nm	449
Zn, 300nm	559
SnO_2, 35-55nm	380
ZnO, 80-200nm	118
Fe, 800nm	380

Table 3: Price comparison for Al_2O_3 nanoparticles [63]

Name	Price for 500 grams / USD
Al_2O_3 alpha, 99+%, 80nm	138
Al_2O_3 alpha, 99.9% 135nm	115
Al_2O_3 alpha, 99.9% 200nm	118
Al_2O_3 alpha, 99.9% 300nm	118
Al_2O_3 alpha, 60nm, Superhydrophobic	298
Al_2O_3 gamma, 99.99%, 5nm	280
Al_2O_3 gamma, 99+%, 20nm	128
Al_2O_3 gamma high purity 99.5% 80nm	239
Al_2O_3 80%alpha/20%gamma, 50nm	228
Al_2O_3 50%alpha/50%gamma, 50nm	358
Al_2O_3 20%alpha/80%gamma, 50nm	358
Al_2O_3 amorphous 50nm	293

Within Aluminum Oxide, there are multiple options based on nanoparticle size, alpha or beta configuration, etc.; there is also an option to buy ready-made nanofluids. The prices for the different variants of aluminum oxide are given in the tables 3.

From table 4 it is clear that buying nanofluids instead of nanoparticles is not cost-effective. The better method is to buy nanoparticles and prepare nanofluids in the lab.

Table 4: Price comparison for Al_2O_3 nanofluid *[64]*

Name	Price for 1 liter / USD
Al_2O_3 in Water, Alpha, 20wt%, 30nm	125
Al_2O_3 in Water, Gamma, 20wt%, 10nm	115
Al_2O_3 in Water, Gamma, 20wt%, 30nm	105
Al_2O_3 in EG, Gamma, 20wt%, 15nm	795

Al_2O_3 nanoparticles of 5nm size are the best candidate from the given option. The purity of these nanoparticles is more than 99.99%. The literature also indicates that smaller size leads to higher thermal conductivity, and for a commercial heat generator, this can be a sought-after performance parameter.

Chapter 3 Methodology

3.1 Introduction

Chapter 3 discusses the experimental procedure, apparatus, and design of heat generator. The heat generator experimental setup consists of a vessel filled with a working fluid that is agitated by an impeller. The One Factor at a Time technique is used to systematically study the impact of different independent factors on the heat generator's performance. The specifications and features of the experimental apparatus are discussed, along with the uncertainty of measurements. Sample preparation of the working fluid is covered along with the experimental procedure used to investigate the temperature rise phenomena. In addition to this, the rationale behind the heat generator's vessel design is discussed by keeping in view previous research work.

3.2 Design and Fabrication of Heat Generator

From the literature review, it is clear that the heat will be generated once the fluid is agitated [13]; this heat will be stored by the fluid if there are negligible losses to the environment. The literature and theoretical analysis indicate that all the mechanical power that goes into the system will be converted into heat as no energy is stored in the energy cascade process [6]. To measure the quantity of this generated heat sensible heat storage formula (16) can be used as both the heat generated by the viscous dissipation and the heat stored by the fluid and container are the same,

$$Q_{stored} = m_{wf} c_{p,wf} \Delta T + m_{cnt} c_{p,cnt} \Delta T \tag{16}$$

Where m_{wf} is the mass of working fluid, $c_{p,wf}$ is the specific heat of the working fluid, m_{cnt} is the mass of steel container, and $c_{p,cnt}$ is the specific heat of the container.

The insulation encloses the heat generator vessel's walls; hence a part of the heat is stored in the mass of vessel walls, hence it is included in the heat storage equation. The following formula measures the power input that goes into the vessel.

$$P = \tau \cdot \omega_{cyc} \tag{17}$$

where τ is the torque measured in $N \cdot m$ and ω_{cyc} is the angular velocity measured in rad/s. If the power is constant during the whole experiment, it can be multiplied by time to obtain kinetic energy. Ideally, this kinetic energy and heat stored should be equal if there is no heat loss to the environment. The energy balance of the process is shown in equation (18).

$$P \cdot t = Q_{stored} \tag{18}$$

The heat generator's design needs to maximize the heat generated by viscous dissipation, and keeping this in mind, the following sections discuss the design and fabrication of the heat generator.

3.2.1 Impellers

The turbulence inside the vessel comes from the stirring of the liquid by the impeller. An impeller is a rotating component that converts the shaft's mechanical energy into hydrodynamic motion [65]. An impeller can be classified by its physical form or operation category. Some commercially available impellers are propellers, turbines, paddles, and high shear impellers [66]. These impeller types can be divided into two major groups depending on the flow regime they create; these flow regimes are axial and radial. The radial flow type impellers apply greater shear stress to the fluid than their axial flow type counterparts. The flow pattern for each type is visualized in figure 3-1.

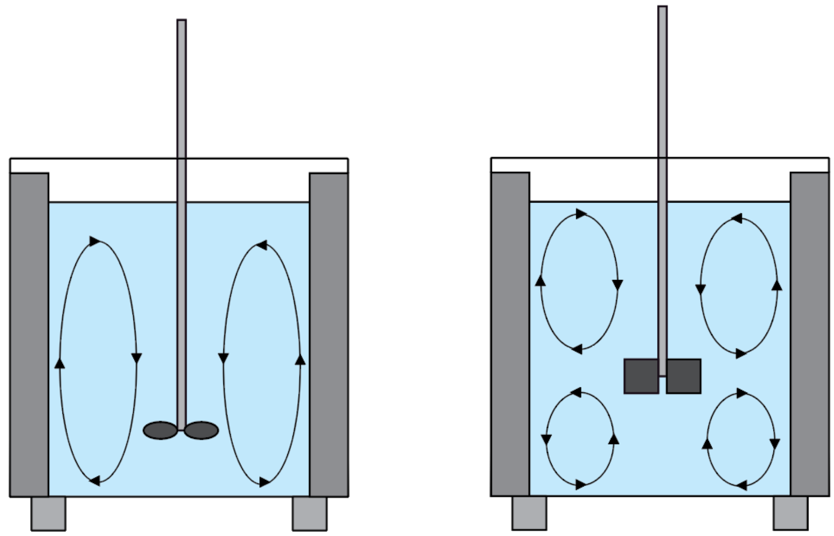

Figure 3-1: Axial flow type (left) and Radial flow type (right) impellers. [67]

The work on impellers' power characteristics goes back more than a hundred and fifty years, with the earliest paper on the subject published in 1855 [74]. While there is no direct mathematical relation that could relate the above-mentioned impellers' power characteristics to obtain a theoretical power equation, there is still much literature on empirical data that could be studied to make qualitative analysis and select the best option for this experimental study.

3.2.2 Dimensionless Analysis

The impeller power consumption is a function of rotational speed, external forces like gravitational force, fluid properties like density, viscosity, along with impeller and vessel geometry. Buckingham pi and dimensional analysis are used to obtain twelve dimensionless groups that can correlate the power consumption in a vessel. The dimensionless groups obtained by Buckingham pi are noted below.

$$f\left(\frac{D^2N\rho}{\mu},\frac{DN^2}{g},\frac{P}{\rho N^3D^5},\frac{D}{D_T},\frac{D}{Z},\frac{D}{C},\frac{D}{p},\frac{D}{w},\frac{D}{l},\frac{n_2}{n_1},\frac{D}{B},\frac{D}{l_b}\right)=0 \tag{19}$$

The equation is by no means universal; it is valid only for a cylindrical vessel with an impeller placed at the center. For multiple impellers or a different tank shape, more dimensionless groups need to be introduced. The first three terms in the equation are Reynolds number, Froude number, and Power number. The equality of these groups ensures dynamic and kinematic similarity between two geometrically similar vessels. The last nine groups of the above equation are responsible for the geometric similarity. It can be observed from the above relation that any number of factors can impact the power consumption of vessels, but it will be seen that some of these factors are more prominent than others.

The Reynolds number is the ratio between inertial and viscous forces, and the Froude number is the ratio between inertial and gravitational forces. These two non-dimensional numbers are well established in fluid mechanics, but the Power number is a relatively lesser-known quantity.

It is useful to note that the power number is analogous to the drag coefficient for an immersed body; this relation helps us understand the power number's physical significance and identify many similarities between the Power number and drag coefficient.

Power number can be derived from the drag coefficient relation by a simple substitution.

$$C_d=\frac{2F}{\rho v^2A} \tag{20}$$

Using the relations $v \propto ND$, $A \propto D^2$, and $P \propto NDF$, the following proportional relations are derived.

$$C_d \propto \frac{P}{\rho N^3 D^5} \tag{21}$$

$$C_d \propto N_p \tag{22}$$

3.2.3 General Correlation Curves

The easiest way to visualize the correlation between the different groups is to plot them on a graph. Plotting all the groups on a graph will make the analysis exhaustive and useless as no useful data can be extracted from that jumbled up graph, so focus is concentrated on the groups responsible for kinematic and dynamic similarity. The following relation summarizes the Reynold, Froude, and Power numbers relationship for a geometrically similar vessel.

$$N_p \propto (Re)^a (Fr)^b \tag{23}$$

From the three groups responsible for kinematic and dynamic similarity, the Froude number's effect is almost negligible for a fully baffled system [66]. This claim can easily be verified from the fact that no vortexes are formed in a baffled system when compared to an unbaffled system. Because the power dissipation of a baffled system is higher than an unbaffled system, the Froude number is disregarded for the remaining of the investigation. With the Froude number’s elimination, the correlation between the Power number and Reynold’s number can be made easily.

It is interesting to note that the Power number for a baffled system becomes constant at a high Reynolds number and the graph shape is very similar to the Coefficient of drag for a sphere when plotted against Reynold’s number [68]. As shown in figure 3-2, the plot between the Power number and Reynold number is a popular choice by many researchers to present their findings. While it is easy to understand and interpret, this graph has led to a widespread misconception that only the Reynold number is needed to conclude the power input needed by a system. It is important to note that this dynamic similarity is only valid for a particular geometric configuration and that any change in any of the geometric parameters will give a different result.

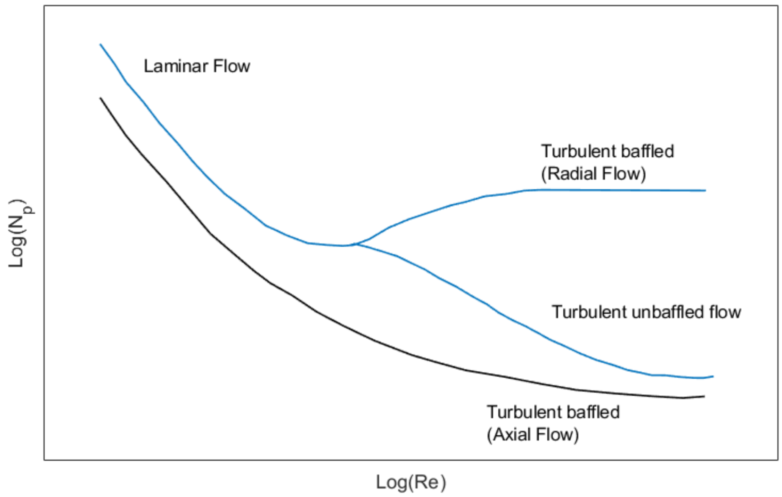

Figure 3- 2:Power Number vs Reynolds number

A monumental paper by Bates et al. [69] conducted a comprehensive comparison among many different radial type impellers. They observed a decrease in power number with an increase in Reynold's number. As the flow becomes fully turbulent, the power number becomes constant [70]. For a given impeller type, as the number of blades, width of a blade, or length of blades increase, so does the Power number. Different types of impellers have different Power numbers, with Rushton turbine having the highest Power number and Flat blade turbine (FBT) coming a close second with only a negligible difference. Any curvature or pitch change of the FBT blade decreases that turbine's maximum power number compared to a generic FBT.

The impeller's position at varying depths of the liquid inside the vessel has a negligible effect on power number for any value above C/D = 1. Bates et al. noted that clearance, on the other hand, impacts the power number. They noted that the difference in performance varies between the different types of impellers where the power number increases with increasing clearance for disk type impeller but decreases for pitched type impeller. For the flat type of impeller, the clearance of C/D = 1 is enough to reach a reasonably high-Power number.

3.2.4 Baffles

In a vessel without baffles, there exist two types of flow regions, for the region around the impeller, the liquid rotates as a whole, and for the region from there to the vessel wall, a free vortex exists. Aiba [71] found that this phenomenon is independent of the type of impeller. He also noted that the flow pattern is independent of impeller speed. This is because, in an unbaffled vessel, the tangential velocity component is high compared to other components.

The introduction of baffles makes the flow more erratic, and hence the vortex are not formed. For a fully baffled vessel, the tangential velocity decreases while the radial velocity remains unchanged [72]. A fully baffled configuration for a given vessel is when the relative Power number of baffled vessels is highest compared to the unbaffled vessel's Power number. The introduction of baffles also increases the Power number of a given impeller [73]. Hence for this experimental study, a fully baffled vessel is used.

Bates et al. [69] conducted experiments with varying lengths of the baffle and varying diameter of FBT and found that the baffle ratio of 0.4 is optimum for any turbine diameter and that any increase in the length of baffle after that point will decrease the power number. Nagata et al. [74] observed the same trend, but they gave 0.5 as the optimum baffle ratio. The baffle ratio is defined as:

$$Baffle\ Ratio = \frac{n_b w_b}{D_T} \tag{24}$$

Where n_b is the number of baffles and $\frac{w_b}{D_T}$ is the ratio of baffle length to tank diameter. If four baffles are used where each baffles length is ten percent of the tank's diameter, this configuration is considered fully baffled.

3.2.5 Design

Guided by the energy balance equation, it is clear that all of the power introduced into the system is converted into heat. The goal of this study is to design a heat generator which would consume high power input. Using the experimental data from the literature the cylindrical configuration is chosen because of ease in manufacturing and the fact that most experimental studies and handbook data is available for cylindrical vessels. The length to height ratio is kept at 1:1. Four baffles each $\frac{1}{10}th$ of the diameter are selected to form a fully baffled configuration. The impeller is flat blade type, and its clearance from the bottom of the vessel is $\frac{1}{3}$ of vessel height. All these criteria are selected to maximize the power input to the heat generator. The heat generator is designed for five liters of volume, and this volume guides the dimensions of the vessel. The engineering drawings of the experimental setup are detailed in the appendix of the thesis.

To investigate the effect of change in diameter, two different impellers are used in the experimentation. Both of these impellers, along with their dimensions, are shown in figure 3-3:

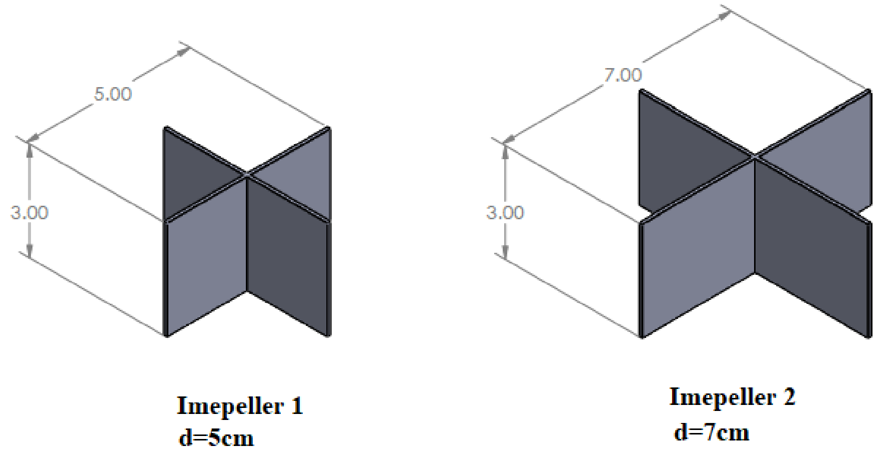

Figure 3- 3: Impellers used in the experimental study.

3.2.6 Fabrication

The heat generator is made of Grade 316 Stainless steel, which is selected due to its corrosion-resistant nature and good mechanical properties. Water jet cutting was used to cut sheets of metal into the required shape, which were then welded together. The heat generator was made in two parts, the bottom part consisted of the vessel, and the upper part consisted of motor and torque sensor housing. Both parts were joined together using mechanical fasteners and clamps. Thermocouples could be inserted through holes on the upper cover of the vessel.

The motor and torque sensor were joined together using Lovejoy Jaw coupling; these couplings are good at tolerating slight misalignment and hence reduces vibration. A standard solid coupling was used to attach the torque sensor with the impeller shaft. The vessel was insulated using Reflectix ® double reflective insulation [75].

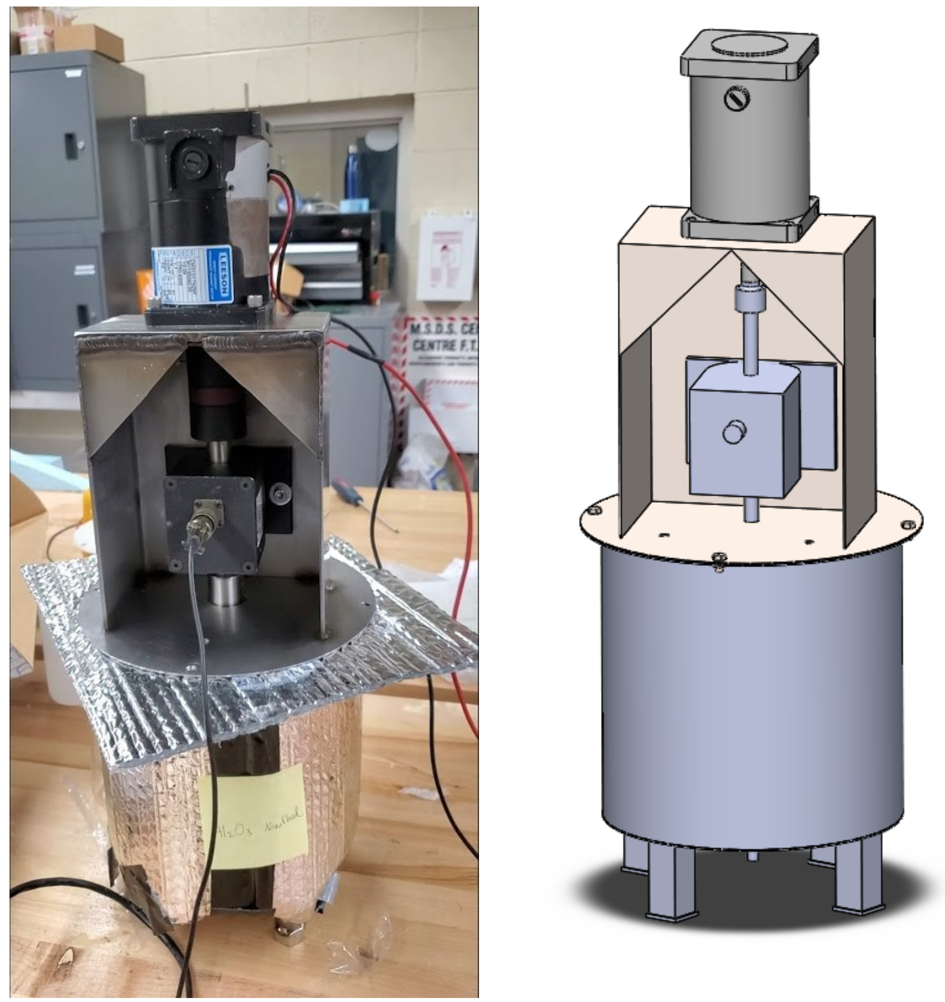

Figure 3-4: a) Experimental Apparatus Pictures. b) CAD Model of Experimental Apparatus.

3.3 Experimental Setup

The heat generator experimental setup consists of a vessel filled with a working fluid that is agitated by an impeller, as shown in figure 3-5. In a commercial prototype, a wind turbine will be responsible for providing kinetic energy, but in this study, the impeller is powered by a DC motor controlled by a speed controller. The electric motor operates at a constant speed for each experiment, and a tachometer is used to record this speed – in rotation per minute (RPM). A torque sensor is attached between the impeller and DC Motor. A data acquisition system records the torque values from the torque sensor and temperature values from the thermocouples. The experimental setup aims to calculate heat generated and power input using temperature, torque, and RPM values.

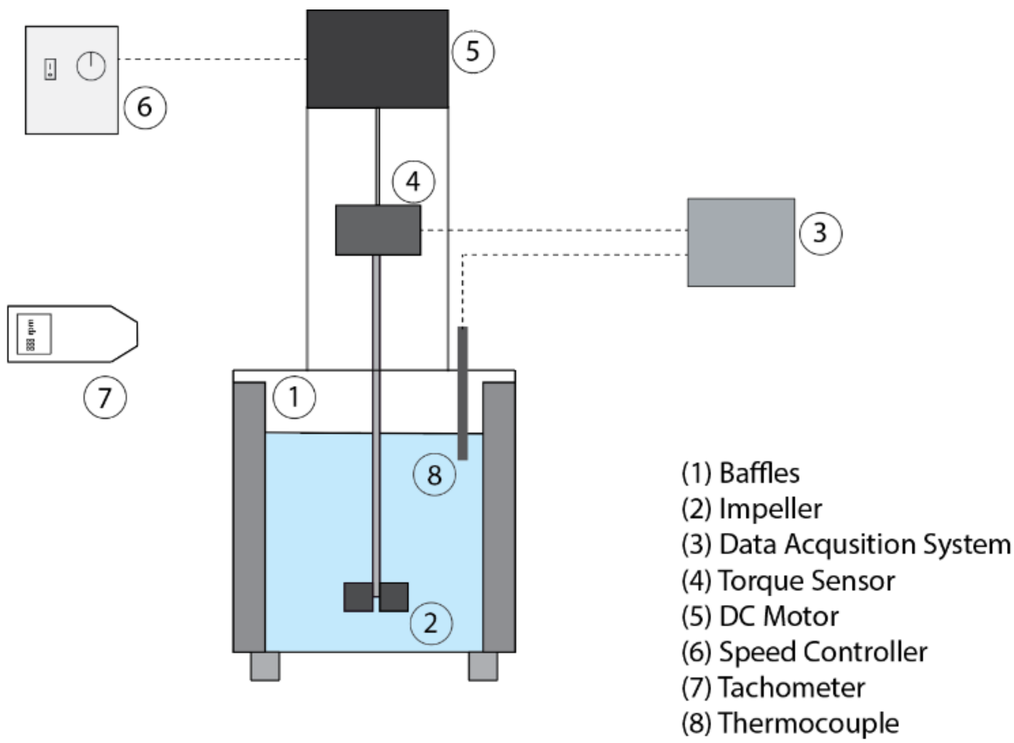

Figure 3-5: Schematics of Experimental Setup.

3.4 Design of Experiment Technique

The experiments are designed to test the device's performance by measuring the increase in working fluid temperature inside the vessel. The two popular choices for conducting experiments are the one-factor-at-a-time (OFAT) method and the factorial methods. The defining difference between both methods is that only one factor is varied in an OFAT experiment, while all the other factors are kept constant. While in the factorial methods technique, multiple factors are varied simultaneously.

Factorial methods have many advantages over OFAT, it can estimate the interaction between different factors, is usually more efficient, and cost less than OFAT for the same amount of data. Nevertheless, at the same time, OFAT is a better choice when the interaction between different factors is not well known. OFAT can give a clearer idea of each factor's impact on the device's performance, and the factorial methods can later be used to optimize the system by building upon OFAT data.

For this study, OFAT is used to vary multiple factors in a series of experiments. This study serves as a proof of concept for this novel idea rather than an optimizing effort for an already established technology; hence OFAT is considered a better choice for experimental design.

3.5 Experimental Apparatus

The experimental apparatus can be divided into three different groups; the first group is the sensors used to record the data from the experiment, the second group is the power supply consisting of motor and speed controller, which provides power to the setup. The last group consists of the data acquisition system, which transfers the data from sensors into the computer.

3.5.1 Sensors

The theoretical analysis tells that five quantities need to be measured and recorded; these quantities are mass, temperature, specific heat, rotational speed, and torque. The torque, rotational speed, and temperature need to be recorded continuously throughout the experiment, which requires a data acquisition system. Keeping in view the expected range of values, accuracy, and budget, the following sensors are selected.

3.5.1.1 Torque Sensor

Torque is a measure of force that causes a shaft to rotate about its axis. While there are two types of torque, reaction and rotational. Rotational torque is investigated for this experimental setup because the shaft is in constant motion. Torque sensors work by converts torque value into an electrical signal with the help of a transducer, strain gauge, bonded to the shaft.

When torque is applied to the shaft, a deflection is induced, which changes the strain gauge's resistance. A Wheatstone bridge converts the change of resistance into an output signal.

Omega TQ513-200 is selected for the experimental setup; this sensor is classified as a shaft-to-shaft rotating torque sensor with an effective range of up to 200 in-lb. It has a full Wheatstone bridge configuration and provides an output signal as mv/V. Omega TQ513-200 is a contact type torque sensor; it uses a silver slip ring to supply power to the transducers and retrieve electrical signals. This sensor supports an excitation voltage of up to 20 Vdc; this excitation voltage is provided by the Data Acquisition System. The effecting operating temperature range is between -54℃ to 121℃, but the compensated temperature range for which the manufacturer guarantees measurement accuracy is between 21℃ to 76 ℃. Because the experiment will be conducted at room temperature, the temperature would not go out of this range.

3.5.1.2 Thermocouples Probe

A thermocouple is a class of sensors that is used to measure temperatures. There are different types available, such as thermocouple wire and thermocouple probe. A thermocouple consists of two types of metals joined to each other with a constant current flowing through its circuit. These two different wires are called thermoelements, and their joining point is called a junction. When the junction is heated or cooled, the temperature difference induces a voltage in the electric circuit. This value of voltage is calibrated to correlate with temperature value using thermocouple curves.

There are multiple thermocouple categories, with type J, K, E, T, E, and N the most common ones. Each of these categories has its operating temperature range and accuracy. For this experimental study, T and J type thermocouples are used in a pair.

The T-type can operate over the range of -250 ℃ to 350 ℃, with the process temperature range of 315 ℃. The thermocouple probe has a stainless-steel sheath material that can protect it from the working fluids. The probe has a diameter of 0.125 inches and a length of 6 inches. This enables it to be inserted from the top end of vessel and saves the trouble of waterproofing the insertion point.

The J-type thermocouple can operate over the range of 0 ℃ to 750 ℃; two probes are used for the experimentation; one of the probes is 6 inches in length while the other probe is 12 inches in length.

A significant reason for choosing probe-type over wire-type is the fact that thermocouple needs to be submerged in a fluid rotating at a very high speed, and in this condition, the probe would be much superior to wire in terms of stability.

3.5.1.3 Tachometer

A tachometer is used to measure the speed of the rotating shaft. The modern digital type of tachometer is optical encoders comprising an LCD readout and a maximum, minimum values storage. The optical encoder's working principle depends on light sources that are reflected on an optical disk. This reflection is recorded by a light detector and converted to an electrical signal.

Contact type and non-contact type are the two main data acquisition techniques. A contact type tachometer is physically connected to the shaft or run by the shaft through a belt, while a non-contact tachometer uses laser or light to read the shaft's rotational speed.

For the experimental study, Lutron DT 2234A Digital Tachometer was used. It has a range of 5-99,999 RPM, with a resolution of 0.1 RPM for < 1000 RPM range. The performance of the tachometer was verified using a Shimpo DT 107A, contact type digital tachometer. Both tachometers gave reading within a 0.5% margin.

3.5.2 Power System

3.5.2.1 DC Motor

Direct Current (DC) motor converts electrical energy into mechanical energy through rotational movement of the shaft. This conversion occurs due to electromagnetism, where a piece of iron is wrapped in a copper wire coil and has voltage applied to it; when this electromagnet is placed between two permanent magnets, attractive and repulsive forces produce a torque. A split-ring commutator and a pair of bushes are used to provide current to the electromagnet and change the current direction so that the motor keeps on rotating.

A brushed permanent magnet DC motor by Leeson that can operate up to 4200 RPM is selected for the experimental setup. It can provide a continuous torque of 0.282 $N.m$ (40.0 in-oz) at its highest speed of 4200 RPM. The operating voltage for this motor is $24Vdc$ and the maximum rated current is 7.7A. According to the manufacturer's specifications, this motor can provide up to 0.07kW continuous power output.

3.5.2.2 Speed Controller

Speed Controller is used for operating DC motor and control its speed [76]. A power supply capable of giving $20V$ and $10A$ output supplies power to the motor through this speed controller. A low voltage DC motor speed controller is used as it supports the required range of voltage and could work well with the DC motor.

The speed controller's voltage ranges 0-24V DC with a maximum current of 16A [77]. These values lie within the operating range of both motor and power supply.

3.5.3 Data Acquisition System

National Instruments Data Acquisition (DAQ) system is used to measure and store the torque and temperature values. The system consists of a chassis with two I/O Modules, one for temperature and the other one for torque. The DAQ chassis is connected to a computer using a USB; the computer runs LabView software which is then used to store the data.

3.5.3.1 CompactDAQ Chassis (NI-9178)

Chassis is responsible for timing, synching, and transfer of data from I/O Modules and computer systems. NI-9178 can support up to 8 input modules concurrently. The input voltage range for the chassis is 9-30V, and it can operate in the temperature range of -20℃ to 55℃. The timing resolution for the model is 12.5ns, making it a very accurate and sturdy DAQ system [78].

3.5.3.2 Temperature Input Module (NI 9211)

NI 9211 is an I/O module for the cDAQ chassis. It has anti-aliasing filters, automatic cold junction compensation, and open detection of the thermocouple. It offers high accuracy and calibration, which is certified by NIST. [79].

3.5.3.3 Torque Input Module (NI 9237)

NI 9237 module can provide power and signal conditioning to bridge-based sensors, which are used to measure torque. It can work with not only full-bridge configuration but also half-bridge and quarter bridge bases sensors. [80].

3.5.4 Differential Scanning Calorimetry (DSC)

Differential Scanning Calorimetry (DSC) study is conducted to determine the specific heat of various working fluids that are used in the experimentation. While the specific heat for Water, Ethylene Glycol, and their mixture are readily available in the literature, there is no credible resource for Nanofluids' specific heat, making the DSC method invaluable.

The equipment used is Mettler-Toledo DSC1, which provides highly accurate values. Furthermore, temperature modulated DSC method ($TOPEM^{®}$) is used, which can separate temperature-dependent and time-dependent processes. TOPEM is the most accurate way to measure specific heat using Mettle Toledo equipment [81].

3.5.5 Uncertainty Analysis

Uncertainty is associated with every kind of measuring instrument. It is virtually impossible to eliminate the uncertainty from an experimental study, which makes it extremely important to know about this uncertainty. The uncertainty value is a guarantee that the real value lies within the range of the reported value. The uncertainties associated with the equipment used in this study are listed in Table 5.

Table 5: Measurement uncertainties

Parameter	Uncertainty
Temperature	± 0.5 ℃
Specific Heat, c_p	$\pm 0.15, J/kg \cdot K$
Torque, τ	± 0.2 lb-in
Mass, g	± 1 gram
RPM	± 0.5 RPM
Volume	± 0.05 liters
Efficiency	Up to $\pm 28.7\%$

The uncertainty of a calculated dependent variable can be calculated from the uncertainties of these independent variables. For example, the uncertainty δR of a value R which is multiple of the independent variables X is given below [82].

$$R = X_1^a X_2^b X_3^c \dots X_M^m \tag{25}$$

Then

$$\frac{\delta R}{R} = \left\{ \left(a \frac{\delta X_1}{X_1} \right)^2 + \left(b \frac{\delta X_2}{X_2} \right)^2 + \left(c \frac{\delta X_3}{X_3} \right)^2 + \dots + \left(m \frac{\delta X_M}{M} \right)^2 \right\}^{\frac{1}{2}} \tag{26}$$

The major dependent variable calculated in this study is the efficiency of energy conversion. The uncertainty associated with efficiency is up to 28% for experiments with lower rotational speeds and higher specific heat fluids, which causes a small temperature rise.

3.6 Working Fluid Preparation

The nanofluid can be prepared using the single-step method or two-step method. The two-step method is selected for the experiments as it was more convenient to get large amounts of nanoparticles from an industrial manufacturer. Nanoparticles were ordered in a dry powder form from the manufacturer US Research Nanomaterials, Inc.

From the literature it's found that researchers have used a variety of methods to disperse the nanoparticles in the base fluid. The most popular method of dispersion for both Water and Ethylene Glycol base fluid is ultrasonication [61] [83-86]. But at the same time, a study is also found where researchers used a combination of ultrasonication, homogenization, and electromagnetic agitation to disperse Aluminum oxide nanoparticles in water [87]. Apart from these, there are also examples from literature where nanoparticles were simply "shaken thoroughly" [88]. Another paper on AlN (Aluminum nitride) nanoparticle noted that a laboratory dissolver stirring at 3000 RPM for 40 minutes gives "high flow-ability and noticeable homogeneity" in nanofluid [89].

Because a large amount of nanofluid needs to be prepared for the experiment, and the fact that the experimental apparatus is a stirring vessel in continuous motion, mechanical stirring for nanoparticle dispersion in the base fluid is selected. The nanofluid's stability is not a serious concern because of the fact that fluid will be homogenous due to continuous mixing.

3.7 Experimental Matrix

In this study, the effect of the base fluid, nanoparticle concentration, impeller diameter, and rotational speed on the temperature rise characteristics and energy conversion efficiency is under investigation. The experimental matrix to investigate these criteria is represented in Table 6.

Table 6: Outline of the experiments under different volume concentrations of nanofluid and impeller RPM values

Experiment Number	Base Fluid	Nanoparticle volume concentration (%)	Rotational Speed (RPM)
1	Water	0	750
2	Water	0.5	750
3	Water	0.75	750
4	Water	1.0	750
5	Water	0	1000
6	Water	0.5	1000
7	Water	0.75	1000
8	Water	1.0	1000
9	EG	0	750
10	EG	0.5	750
11	EG	0.75	750
12	EG	1.0	750
13	EG	0	1000
14	EG	0.5	1000
15	EG	0.75	1000
16	EG	1.0	1000
17	EG: Water (20:80)	0	750
18	EG: Water (20:80)	0	1000
19	EG: Water (50:50)	0	750
20	EG: Water (50:50)	0	1000
21	EG: Water (80:20)	0	750
22	EG: Water (80:20)	0	1000
23	Water (Impeller 2)	0	750
24	Water (Impeller 2)	0	1000

There are three different base fluids, three different concentrations of nanoparticles, two different diameters of impellers, and two different rotational speeds used in this study.

The volume concentration is going to be calculated using the formula (27) [90]:

$$\phi = \frac{\left(\frac{W_{nf}}{\rho_{nf}}\right)}{\left(\frac{W_{nf}}{\rho_{nf}} + \frac{W_{bf}}{\rho_{bf}}\right)} \tag{27}$$

According to the manufacturer of nanofluid, the density of nanofluid is 3890 Kg/m^3 [91]. The density of water is 1000 Kg/m^3 and density of ethylene glycol is 1.1132 Kg/m^3 . Using these densities, the mass required to make a certain volume concentration of nanofluid can be easily calculated. Table 7 details the mass of nanoparticles required for the nanoparticle concentration.

Table 7:Mass of Al_2O_3 Nanoparticle needed to make 5 liters of required Volume Concentration of nanofluid.

Volume Concentration (%)	**Mass of Al_2O_3Nanoparticle**
0.50	97.74 g
0.75	146.98 g
1.00	196.46 g

3.8 Summary

In this chapter, the theory behind the experimental design of the heat generator was discussed. The one-factor-at-a-time (OFAT) method was selected to conduct the experiments because of the study's preliminary nature.

Experimental apparatus was also discussed, including sensors, data acquisition system, power system, and DSC setup. The working principle of the equipment was described along with the rationale behind choosing that particular equipment.

Details regarding the design and fabrication of the heat generator were discussed. Different factors were identified, and the design of the heat generator was optimized by selecting impeller, baffles, and geometric configurations that would maximize the heat generation. The sample preparation of nanofluids, their economic analysis, and the experimental procedure was discussed at the end.

Chapter 4 Experimental Results and Analysis

4.1 Introduction

In this chapter OFAT approach is used to conduct the experiments on the heat generator. The torque value on the impeller shaft and temperature rise in the heat generator's fluid for varying rotational speeds, base fluids, nanoparticles' volume concentrations, and impeller diameter are recorded and analyzed.

4.2 Signal Filtering of Torque Data

The output signal from the torque sensor is conveyed to the DAQ system using a shielded wire. The output of the torque sensor is in mV and not in the familiar $N \cdot m$ or $lb \cdot in$ units. This conversion from mV to $N \cdot m$ or $lb \cdot in$ is achieved using the calibration charts provided with the torque sensor. Once inside the LabView setup, these calibrated values are used to calculate the final output.

Even with shielded wires, the torque sensor is prone to electromagnetic interference from the DC motor and electronics in the laboratory. In addition to this, mass imbalance in the shaft leads to cyclic load which is picked up by the torque sensor. This cyclic load and electromagnetic interference lead to noise in the output signal, which needs to be filtered before the torque value is used in further analysis.

To verify the performance of the torque sensor under no electrical, magnetic, or mechanical interference, a static torque was applied to the shaft, and the toque value was recorded. The output had almost no noise as all electrical equipment was turned off, and there was no cyclic load as the shaft was stationary. When this data was plotted on the frequency domain, data was output at 0

Hz, or in other words, the output of the torque sensor was found to be not cyclic at all.

Hence, data at any frequency higher than 0 Hz is noise and needs to be eliminated to have accurate results. Once the higher frequency signals are determined to be noise, a low pass filter can be implemented to eliminate this noise. This filter would allow lower frequencies to pass and block out any higher frequencies from the raw signal. There are two ways of implementing a filter, first is designing and installing a physical low pass filter in the experimental setup's circuitry, and the second option is to implement a digital low pass filter on the raw signal. The digital low pass filter is easier to design, implement, and cost virtually nothing, so for the purpose of this study, a digital low pass filter was selected to filter the raw data coming from the torque sensor. A finite impulse response (FIR) equiripple filter is implemented in MATLAB to filter out the high frequency data. The F_{pass} of the filter is $1Hz$ and F_{stop} of the filter is $0.5Hz$, these values were selected for stability of the digital filter.

The raw signal for one of the experiments is shown in Figure 4-1(a) to understand the signal filtering significance. It is clear that the value fluctuates violently between the maximum and minimum values and the range is too great to ignore. The same data is presented in the frequency domain in Figure 4-1(b). The frequency-domain figure shows that the peak is at 0 Hz, followed by smaller peaks at 16.6 Hz and 33 Hz. There is much noise in the 0 Hz – 5 Hz region as well.

Interestingly, the peak at approximately 16.6 Hz corresponds to the setup's mechanical vibration; for example, the motor was operating at 1000 RPM, which is 16.67 RPS or 16.67 Hz. This phenomenon indicates mass imbalance as noise frequency is the same as running RPM [92]. The noise at lower frequencies is due to electromagnetic interference.

It can be concluded from this discussion that the frequency pass region should be as small as possible; hence a digital filter is designed that lets in signals with less than 0.5Hz frequency. The filtered data is plotted in Figure 4-1(c), and it can be observed that after applying the filter, noise is eliminated from the data, and the result compares well with the expected result (constant torque).

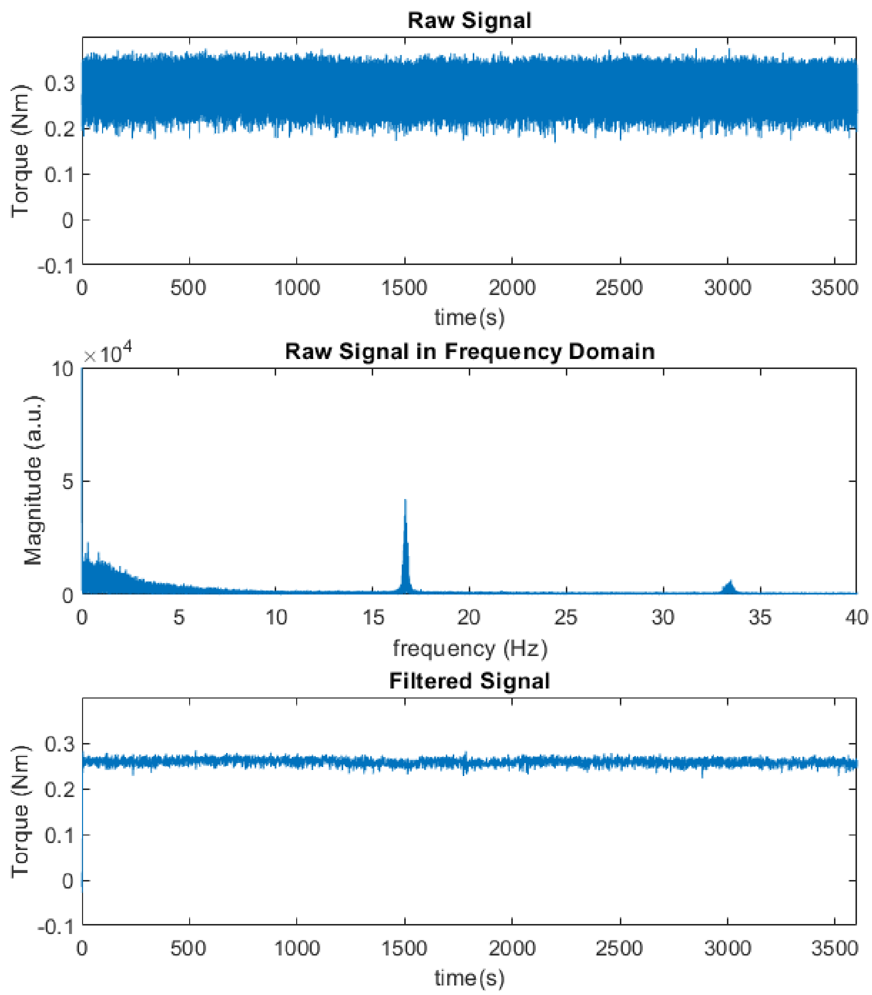

Figure 4- 1: a) Raw signal in time domain, b) Raw signal in Frequency domain, c) Filtered signal in time domain.

4.3 Differential Scanning Calorimetry (DSC) Measurements

Differential Scanning Calorimetry measurements were conducted to measure the specific heat of nanofluids. Specific heat value is very important for the analysis later on in the chapter. As stated in formula (16) specific heat values along with temperature rise values will be used to calculate the heat generated due to viscous dissipation. It was concluded in chapter 2 that literature did not have any work on the specific heat values of the nanofluids used in this study. In addition, all the models used to estimate specific heat were awfully inadequate and could not be used for any meaningful analysis.

The DSC results for water-based nanofluids are shown in Figure 4-2. To gauge the DSC equipment's accuracy, an experiment was run on water. The specific heat value from the experiment is plotted in Figure 4-2 along with the values from the literature. The specific heat value calculated by the DSC method is in close agreement with the value from the literature, testifying to the DSC method's reliability.

For the nanofluids, the specific heat for 0.50% Al_2O_3-Water nanofluid was higher than water, and the specific heat value decreases with the addition of more nanoparticles. The lowest specific heat is for 1.00% Al_2O_3-Water nanofluid. This mechanism behind the increase and then the decrease in specific heat with nanoparticles' addition is widely reported in other studies [93] [94] , but it is not understood properly. Some researchers suggest that the nanolayer's presence surrounding the nanoparticles is responsible for this increase in heat capacity at lower volume concentration, but this theory is not widely accepted. [94]

From the experimental results, it can be seen that the specific heat decreases with the increase of temperature; while this trend is expected as evident from the literature the effect is more pronounced in this study, it seems that mass loss is responsible for this exaggerated trend, but overall, the difference is within the margin of error expected from the equipment.

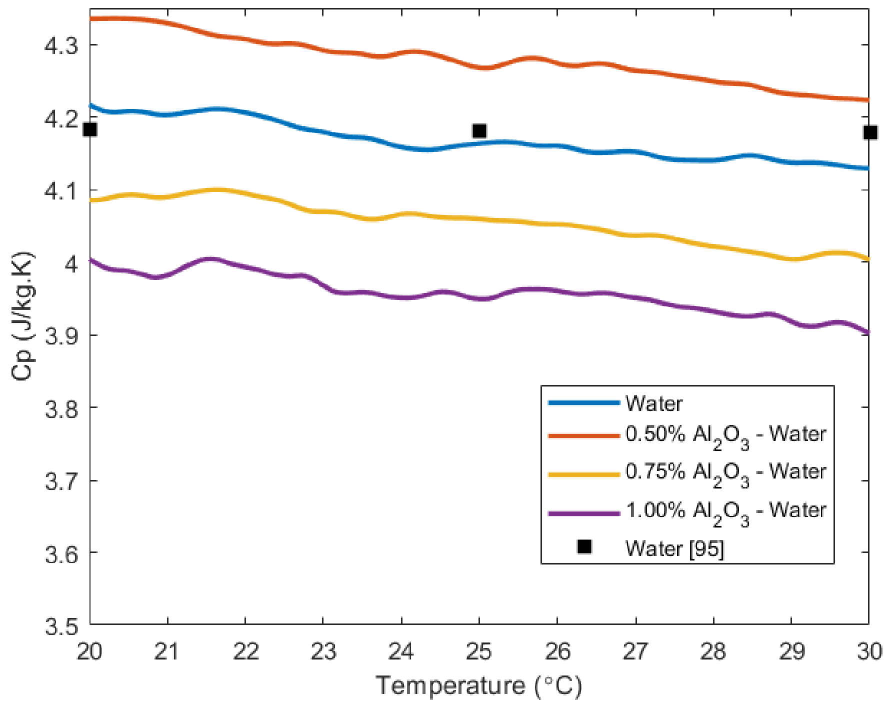

Figure 4-2: DSC results for water based nanofluids

The DSC results for the EG based nanofluids are presented in Figure 4-3. The DSC values for EG are not in close agreement with values from the literature; this is because EG used in the experiments is not one hundred percent pure and contains trace elements of impurities, while the specific heat values for EG that are found in the literature are for pure EG itself. One valuable takeaway from comparing DSC values for EG to literature values is that both of their rate of change with increasing temperature is near identical; this trend is expected as there was no mass loss during EG experimentation on DSC equipment. This further testifies to the fact that the equipment is reliable and accurate in its readings.

For the nanofluids, the specific heat for 0.50% Al_2O_3-EG nanofluid was higher than EG, but the specific heat value decreases with the addition of more nanoparticles. The lowest specific heat in this series is for 1.00% Al_2O_3-EG nanofluid. This trend is similar to water-based nanofluids' data. From the experimental results, the specific heat for the nanofluids slightly increases with the increase of temperature.

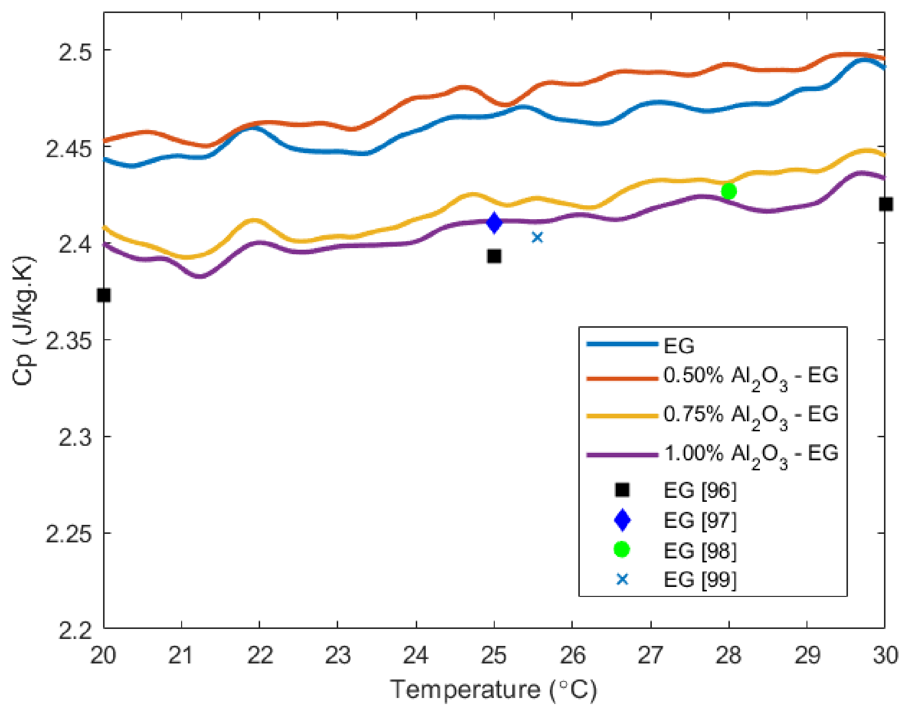

Figure 4-3: DSC results for EG based nanofluids.

With the DSC experiments, a reliable set of specific heat data for nanofluids is measured.

4.4 Thermal Conductivity and Viscosity

In addition to specific heat, thermal conductivity is also an important nanofluid property that will dictate a commercial heat generator's heat transfer characteristics. However, as this study only focused on the heat generation and not the heat transfer aspect of the heat generator, thermal conductivity values were not experimentally measured.

The viscous dissipation was found to be proportional to the fluid's viscosity as seen in the equation (4). Nevertheless, it will be seen in the next section that the viscosity is not as important for the heat generator's performance as it was initially thought. It is for this reason viscosity of the nanofluids is not experimentally investigated.

4.5 Temperature Measurements

4.5.1 Water-based Al_2O_3 nanofluid

The first series of experiments were conducted with water as base fluid and with varying concentrations of nanofluids. Recall Table 6 for the overall experiment matrix. In total, eight experiments were conducted with the water-based nanofluids. Temperature rise data and torque value for four different concentrations (0.00%, 0.50%, 0.75%, 1.00%) of nanofluids at two different rotational speed (750 RPM, 1000 RPM) were recorded.

Figures 4-4 and 4-5 shows the temperature increase of liquid inside the vessel within 60 minutes of fluid agitation. It can be noted that the temperature increase is almost linear. The final value of temperature rise at the end of the experiment is not statistically significant to indicate that nanoparticle's changing concentration has any effect on temperature rise.

For the 750 RPM rotational speed experiments, the temperature value range at the end of the experiments for all the nanofluid concentrations is within the ± 0.12 °C. The average increase in temperature was noted to be 2.1 °C.

In the 1000 RPM rotational speed experiments, the temperature value range at the end of the experiments for all the nanofluid concentrations is within ± 0.50 °C. The experiment with

0.75% Al_2O_3 had a slightly lower temperature rise than other experiments, but the average total temperature rise was around 4.35 ℃.

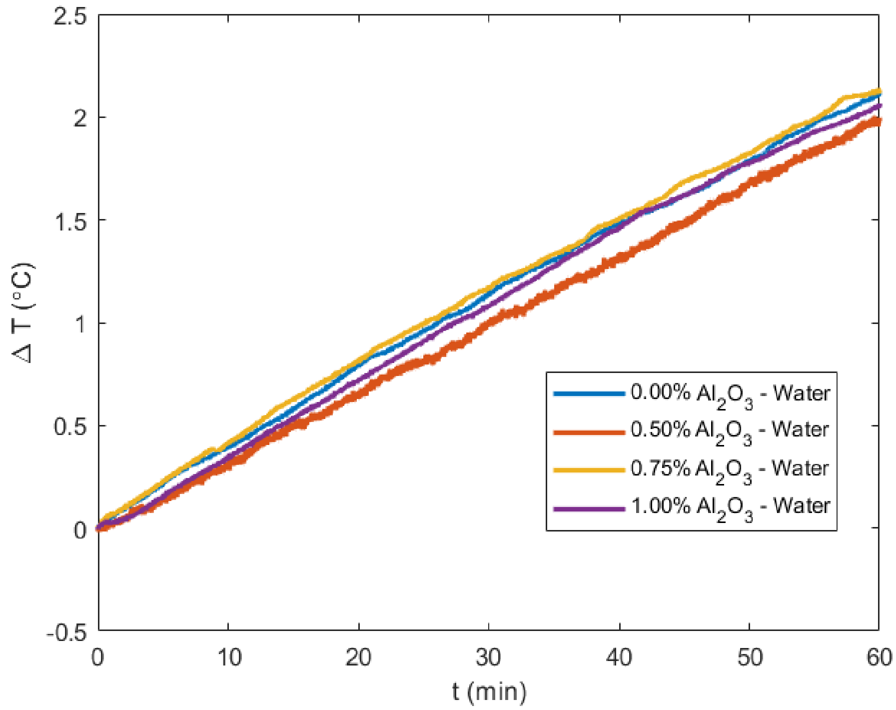

Figure 4- 4: Al_2O_3-Water *nanofluid* temperature increase at 750 RPM.

The linear temperature rise is expected because the power input that goes into the vessel through the impeller's rotation is constant throughout the experiment. From Equation (16), it becomes clear that for a constant mass and near-constant specific heat, a linear rise in temperature for constant power input is expected. Although the specific heat of a fluid is a function of temperature and varies slightly with the change in base fluid temperature, this change is not significant enough to have any measurable effect.

The correlation between temperature rise and rotational speed becomes clear from Figures 4-4 and 4-5. Higher rotational speed corresponds to higher temperature rise and vice versa.

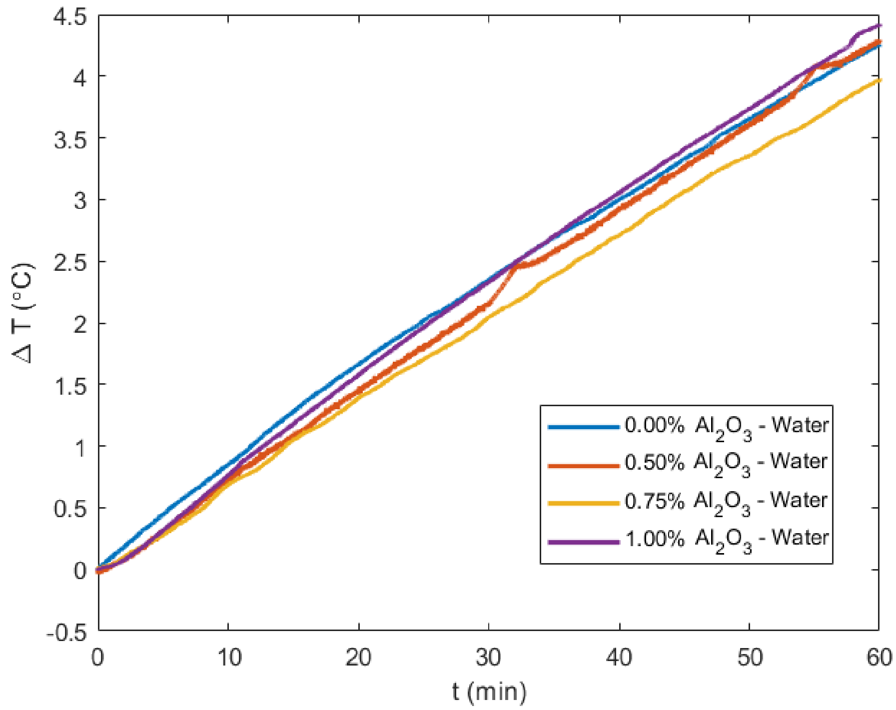

Figure 4-5: Al_2O_3-Water *nanofluid* temperature increase at 1000 RPM.

4.5.2 Ethylene Glycol (EG) based Al_2O_3 nanofluid.

The second series of experiments were conducted with Ethylene Glycol (EG) as base fluid and with varying nanofluids concentration, just as in the last subsection. In total, eight experiments were held in EG based nanofluids with four different concentrations (0.00%, 0.50%, 0.75%, 1.00%) of nanofluids and two different rotational speed (750 RPM, 1000 RPM).

Figures 4-6 and 4-7 show the temperature increase of liquid inside the vessel within 60 minutes of fluid agitation. Just as the last subsection, the temperature increase is almost linear, and the final value of temperature rise at the end of the experiment is affected only slightly by changing nanofluids' concentration.

For the 750 RPM rotational speed experiments, there is an almost identical temperature rise trend for pure EG and 0.5% Al_2O_3– EG Nanofluid. For 0.75% and 1.00% concentrations, the final temperature rise decreases slightly.

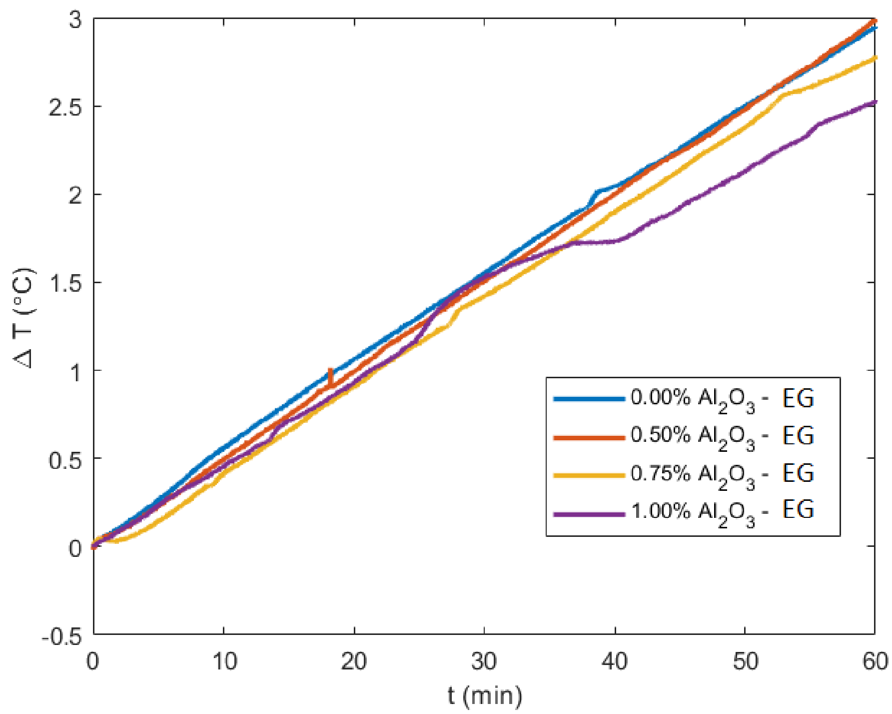

Figure 4- 6: Al_2O_3-EG *nanofluid* temperature increase at 750 RPM.

In the 1000 RPM rotational speed experiments, the temperature rise increases slightly for 0.50% Al_2O_3 -EG nanofluid compared to pure EG. However, with increasing nanoparticle concentration, the temperature rise starts to decrease ever so slightly. Nanofluids' addition does change the temperature rise trend, but the change is insignificant and does not make economic sense. For this reason, nanofluids are not suggested for the commercial development of heat generator due to the high cost of nanoparticles and insignificant temperature rise benefits.

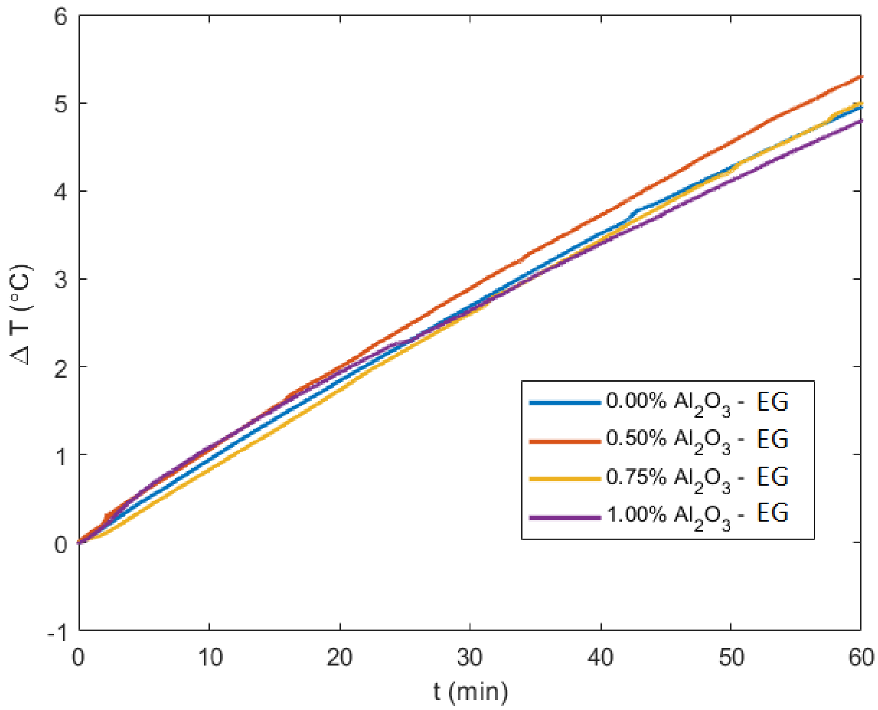

Figure 4-7: Al_2O_3-EG *nanofluid* temperature increase at 1000 RPM.

4.5.3 Effect of Base fluid on temperature rise

The next series of experiments was conducted with a few different Water and EG mixtures as base fluid. In total, five different base fluids are used: Pure Water, Pure EG, and three mixtures of Water-EG in varying percentages, e.g., 20:80, 50:50, 80:20. The rationale behind choosing multiple base fluids is to identify the temperature rise trend and total energy conversion efficiency with varying fluid properties like viscosity and specific heat.

Figures 4-8 and 4-9 show that the rate of temperature rise changes for different base fluids. The highest temperature rise is for pure EG solution, and the temperature rise starts to decrease as the percentage of water in the mixture increases. The lowest temperate rise is observed for 20% EG and 80% Water mixture. The temperature rise difference can be easily explained when specific heat value from table 8 are taken into account; the fluid with the lowest specific heat has the highest temperature rise and vice versa. The only exception to this rule is pure water, which has the second-lowest temperature rise instead of the lowest temperature rise. This is due to the fact that the efficiency of energy conversion for pure water is much higher than that for 20% EG and 80% Water mixture, as clearly seen in figure 4-12.

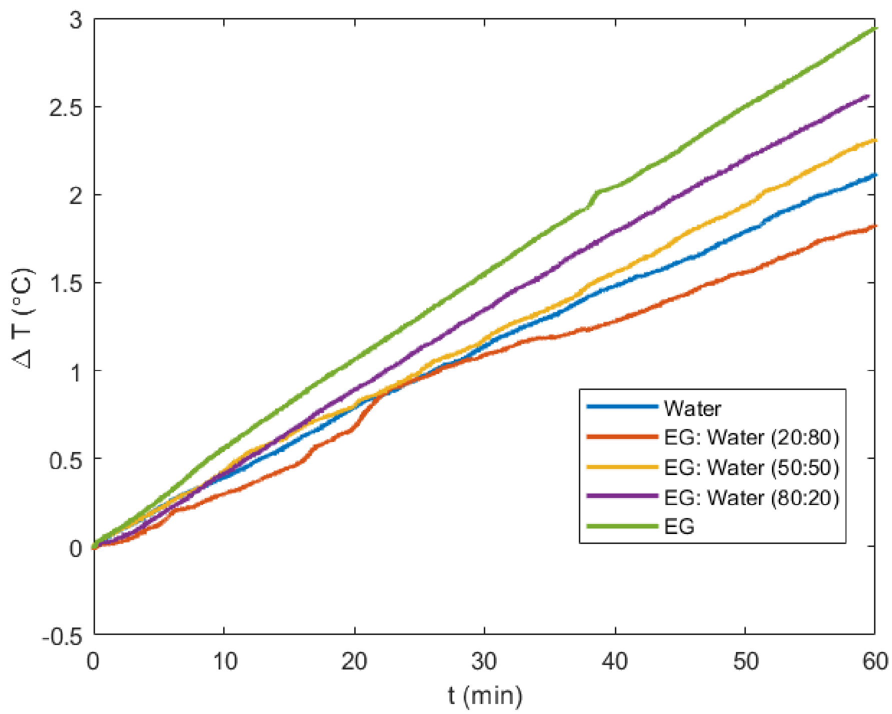

Figure 4-8: Water, EG, and Water-EG mixture's temperature increase at 750 RPM.

Table 8: Specific Heat values for base fluids

Fluid	C_p $(J/kg \cdot K)$
Water	4.18
EG/Water (20:80)	4.03
EG/Water (50:50)	3.64
EG/Water (80:20)	3.06
EG	2.45

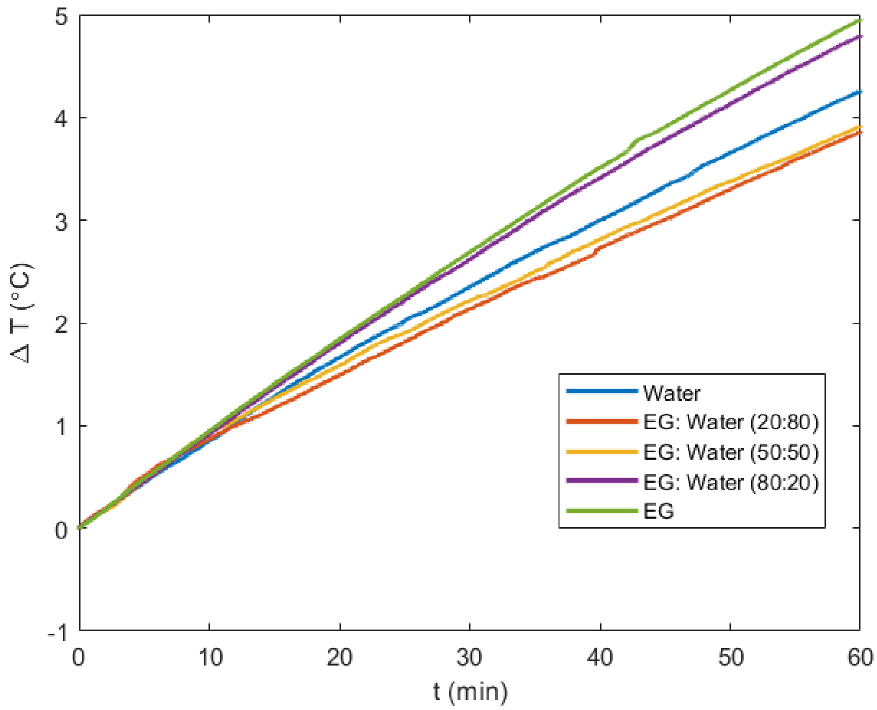

Figure 4-9: Water, EG, and Water-EG mixture's temperature increase at 1000 RPM.

4.5.4 Effect of impeller diameter on temperature rise

Experiments were conducted to better understand the impact of the impeller's diameter on the fluid's temperature rise. The impeller used until this point had a 5 cm diameter; this diameter was increased to 7cm, and experiments were run in water as base fluid. The temperature rise data for 750 RPM and 1000 RPM are represented in Figures 4-10 and 4-11, respectively. It can be observed that temperature rises for impeller with larger diameter increase for both rotational speeds. This trend is in line with theoretical analysis as discussed in formula (22), where an increase in diameter increases the impeller's power number, and hence the system consumes a greater power.

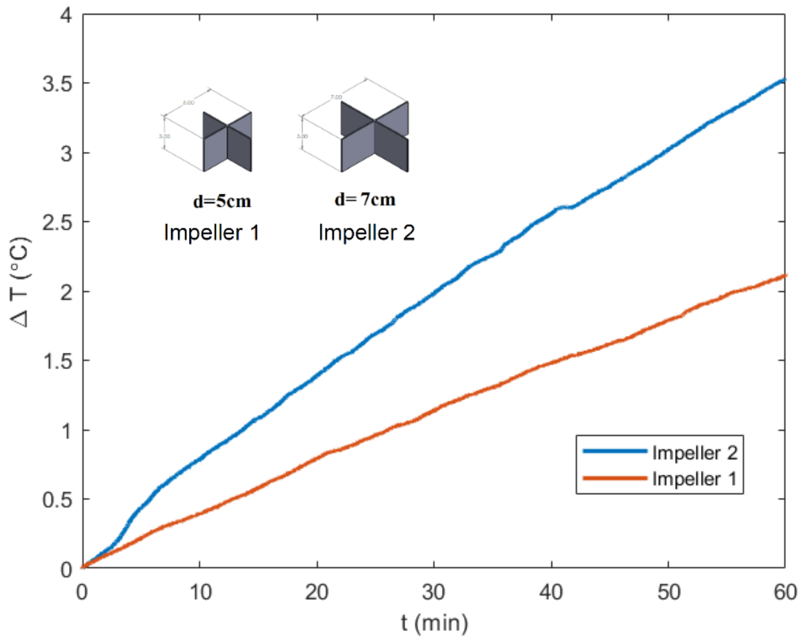

Figure 4- 10: Impeller 1 vs Impeller 2 temperature increase at 750 RPM.

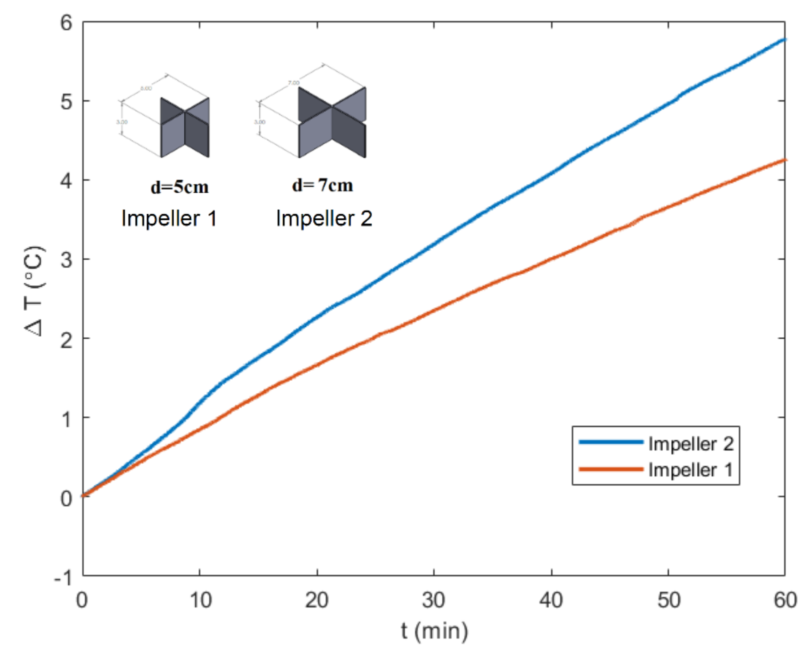

Figure 4-11: Impeller 1 vs Impeller 2 temperature increase at 1000 RPM.

4.5.5 Comparison of temperature rise after 60 minutes.

The temperature rise in the vessel after 60 minutes of fluid agitation is plotted below in figure 4-12 to summarize this section. Figure 4-12 shows that temperature rise is highest for the EG-based nanofluids, and its lowest for water-based nanofluids, with a mixture of base fluid in between. It is also clear that temperature rise is always higher for the higher rotational speed and the bigger impeller diameter.

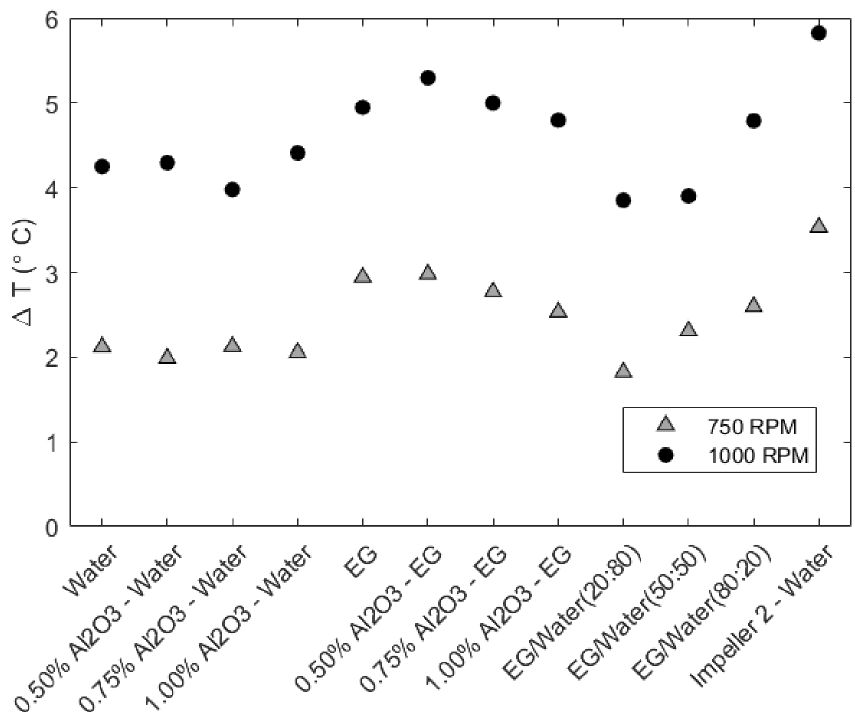

Figure 4-12: Temperature rise after 60 minutes of fluid agitation.

4.6 Efficiency of the Heat Generator

The final step of heat generator analysis is to calculate its efficiency of kinetic energy to heat (or thermal energy) conversion. This analysis looks at the sensible heat energy, as it is easily quantifiable from temperature rise data. Efficiency is defined as:

$$\eta = \frac{mc_p \Delta T}{\tau \cdot \omega_{cyc}} \tag{28}$$

The efficiency of all the experiments is plotted in Figure 4-13. The first eleven experiments plotted are for impeller 1, while the last experiment is for impeller 2. It can be seen that the energy conversion process is highly efficient where some experiments had an efficiency of more than 90% and even the least efficient experiments had an efficiency of 70%.

It is also clear that energy conversion efficiency is almost always higher for 750 RPM, low rotational speed conditions. There are only two experiments where efficiency for 750 RPM and 1000 RPM is almost the same, but it is never higher for 1000 RPM conditions.

Another trend to come out of this analysis is that the efficiency of energy conversion for water-based nanofluids is higher than EG-based nanofluids, and the efficiency of mixture base fluids are in between.

It can also be noted that the efficiency of an impeller with a bigger diameter is lower than the conversion efficiency for a smaller diameter impeller even if other conditions are kept the same.

All these trends can easily be explained when it is realized how the efficiency is defined (28); for this analysis, only the sensible heat energy is calculated using temperature rise data and the latent heat energy is ignored. At the same time, the actual efficiency is stated below in (29), where h is the specific latent heat of vaporization.

$$\eta = \frac{mc_p \Delta T + m_{loss} h}{\tau \cdot \omega_{cyc}} \tag{29}$$

The cavitation process is the culprit due to which 100 percent energy conversion of kinetic energy into sensible heat energy is not observed. Cavitation occurs when the local pressure of liquid goes below the vapor pressure of the liquid. This causes the change in state for the liquid, which then converts into gas. This vapor production process requires a large amount of energy (the latent heat of evaporation). This energy is absorbed from the surrounding liquid and causes the local temperature to decrease. This phenomenon is called the thermal effect of cavitation [100]. In this study impeller is operating at a high rotational speed, which causes the local pressure of the nanofluids and base fluids to go below their vapor pressure, hence causing the change in state.

The vapor pressure of water at 25℃ is 3.17 KPa [101] while the vapor pressure of EG at 25℃ is 0.012 KPa [102], so it can be argued that cavitation is induced at lower pressure for EG compare to water, hence causing lower efficiency as defined in (28).

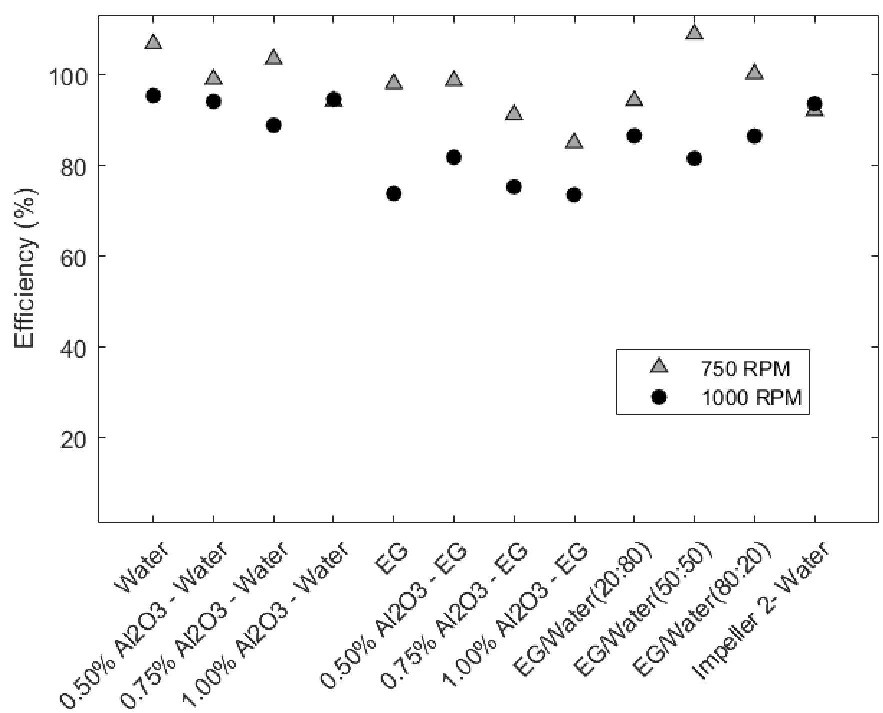

Figure 4-13: Percentage Efficiency of energy conversion.

Another data point to support this reasoning is that efficiency for a larger impeller is always lower than a smaller impeller's efficiency. The bigger impeller induces higher cavitation as it causes lower local pressure compared to the smaller diameter impeller.

Overall, the experimentation points toward the fact that almost all of the kinetic energy is converted into the heat energy, and the conversion is in line with what is expected from theoretical analysis as seen in equation (18).

4.7 Torque Values

This study looked at the temperature rise data and the energy conversion efficiency, but it did not discuss the energy input that goes into the system. Although the power input values were used in the efficiency calculation, it would be worthwhile to look at the vessel's power consumption characteristics to have a complete understanding of factors affecting power dissipation.

The torque and rotational speed values can be used to calculate the power input of the system. The RPM value is kept constant at 750 RPM or 1000 RPM, and only the torque value could vary across the experiments. In Figure 4-14 the torque values for all the experiments using the standard 5cm diameter impeller are plotted. The torque values for non-standard 7cm diameter impeller were 0.299 Nm for the 750RPM experiment, and 0.360 Nm for the 1000RPM experiment. Experimental results of the larger impeller are not included in the figure as these experiments had a different geometric configuration, and comparing those values will not yield any meaningful insight.

The torque value is higher for higher rotational speed. It is also interesting to note that torque values, and consequently the power input is almost constant across all the eleven experiments for 750 RPM rotational speed and 1000 RPM rotational speed. It can be inferred from the data that power input is independent of fluid properties and depends on the geometric values of the vessel and impeller. It is also clear that if one is interested in increasing the vessel's power input, the best way is to focus on the vessel's geometric optimization and not on the fluid property optimization. This is not to say that base fluid is not important, as fluid properties guide the vessel's heat transfer characteristics, and a mix and match of both geometric optimization and fluid optimization are needed for the best performance of the heat generator.

Some of the ways in which a heat generator can be optimized include: increasing the impeller's diameter, using an impeller with a high power number, and using a fully baffled configuration.

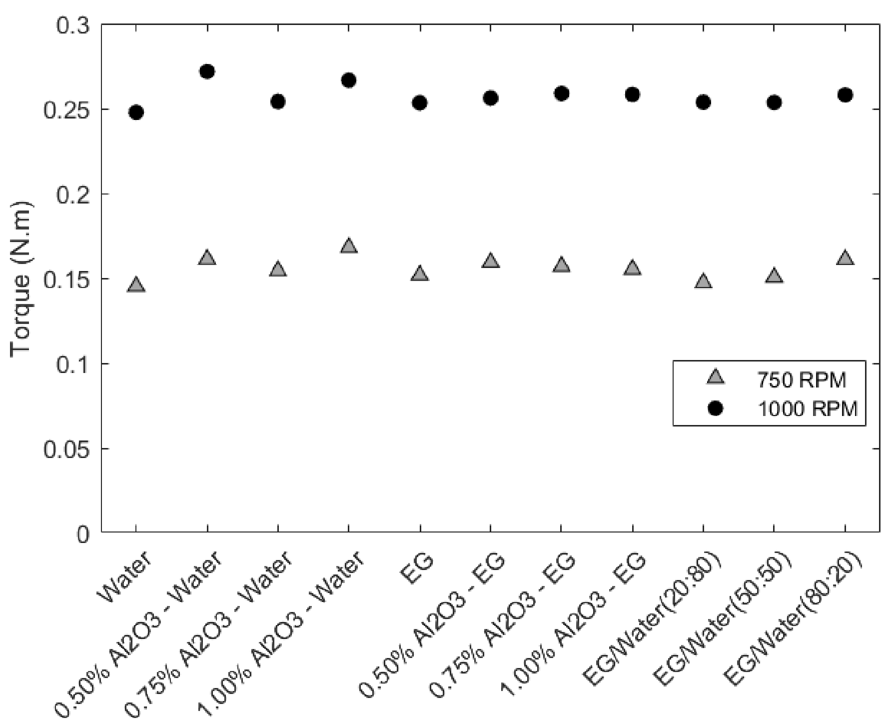

Figure 4-14: Torque Value

4.8 Economic Analysis

This study is academic in nature, but the heat generator developed in this thesis can be easily modified and used for commercial purposes. For that reason, a fundamental Levelized Cost Of Energy(LCOE) analysis is conducted for the system consisting of a heat generator and a wind turbine. LCOE method is used to find the net present cost of energy produced by a power generating plant. Usually, it is used to calculate the cost of electricity, but there is nothing in the method that cannot be modified to analyze non-electricity producing equipment. The formula used to calculate LCOE is given below (27).

$$LCOE = \frac{Net\ Present\ of\ Total\ Cost}{Net\ Present\ of\ Total\ Energy\ Output} = \frac{\sum_{t=1}^{n} \frac{I_t + M_t}{(1+r)^t}}{\sum_{t=1}^{n} \frac{E_t}{(1+r)^t}} \tag{30}$$

I_t is the initial investment, M_t is the maintenance cost, E_t is the energy generated for the year t. The term r is the discount rate, and n is the expected years of operation for the device.

A few assumptions are made to analyze the heat generator system; while the manufacturing cost for the heat generator is known, the wind turbine cost is assumed by looking at a few commercially available options. A 2000 Watts vertical axis wind turbine is selected and capacity factory is assumed to be 25%. The self starting limitations of vertical axis wind turbine are ignored for the purpose of this analysis as it is out of scope of this research. The gearbox can be used to achieve high rotational speeds. A few of these advantages of using this system include:

- A heat generator system operates and generates heat at every wind speed, while a traditional wind turbine can only operate between cut-in speed and cut-out speed region.
- Heat generator can be deployed in regions with extremely high wind speed where a traditional wind turbine cannot operate.

- The efficiency of heat generator is higher than the efficiency of the electricity generator.
- A commercially manufactured heat generator will cost much less than its comparative electricity generator.

The cost of the proposed wind powered heat generator system is given in Table 9. The manufacturing cost values are what it cost to make the prototype on which this experimental study was conducted. While the fabrication cost will be much lower for a commercially produced heat generator, these higher values are used for analysis to be on the safer side.

Table 9: Cost of Wind Powered Heat Generator System

	Cost
SS316 Sheet	$400
Water Jetting	$150
Fabrication	$565
Nanofluids	$355
Gearbox	$500
Installation and Integration	$500
Shanghai Sihao FS-V-2000	$2200

These costs can be used to conduct LCOE analysis as shown in Table 9. A maintenance cost of $100 and its 2% increase is assumed per year. The discount rate is assumed to be 5% to calculate the present value of cost and power. If the device has a life of 10 years, the LCOE is found to be 14 cents per kWh. This value on par with the average rate of electricity in Canada, which is 17.4 cents per kWh [103].

It is reasonable to assume that the wind-powered heat generator system is commercially viable and can be implemented in Canada's windy areas.

4.9 Summary

This chapter presents the experimental results of the study. Temperature rise data for Water-based and EG based Al_2O_3 nanofluids are analyzed, and a proof of concept for heat generator is successfully demonstrated. In addition, DSC experiment data for specific heat values of nanofluids are discussed. In the end, the energy conversion efficiency is detailed along with a short economic analysis of the proposed wind powered heat generator system.

The temperature rise may seem modest but it can easily be increased by using a smaller mass of base fluid. The main take away from this research is the high efficiency of the process. If the power input to the system is large enough, a large amount of useful energy can be extracted from the system.

Table 10: LCOE Analysis

	Year 1	Year 2	Year 3	Year 4	Year 5	Year 6	Year 7	Year 8	Year 9	Year 10
Initial Investment ($)	4670.00	-	-	-	-	-	-	-	-	-
Maintenance Cost ($)		100.00	102.00	104.04	106.12	108.24	110.41	112.62	114.87	117.17
Present Value of Cost ($)	4670.00	90.70	88.11	85.59	83.15	80.77	78.46	76.22	74.05	71.93
Yearly Power Output (kWH)	4380.00	4380.00	4380.00	4380.00	4380.00	4380.00	4380.00	4380.00	4380.00	4380.00
Present Value of Output (kWH)	8760.00	3972.79	3783.61	3603.44	3431.84	3268.42	3112.78	2964.56	2823.39	2688.94

Net Present Value of Total Cost ($)	5398.99
Net Present Value of Total Output (kWh)	38409.77
LCOE ($/kWh)	0.14

Chapter 5 Conclusion and Recommendation

5.1 Conclusion

The conversion of kinetic energy directly into heat energy is a fundamental phenomenon of nature, but this phenomenon was never seriously considered for commercialization or any practical usage. This study is one of the first experimental investigation on the conversion of kinetic to thermal energy. A heat generator was designed, manufactured, and experimentally investigated. An electric motor powered this heat generator. Throughout this research, the following conclusions were identified:

- The theoretical conversion of kinetic energy into heat energy in a closed system is a hundred percent. From this study's experimentation results, it is clear that more than 90% of the kinetic energy is converted into sensible heat energy in the absence of cavitation.
- The cavitation may damage the impeller and evaporates the liquid, which then escapes the system as vapors. Hence, cavitation must be avoided for the best results.
- When a constant power is supplied by an electric motor, the power dissipation is independent of the fluid properties, and it is only dependent on the geometric parameters of the vessel. The geometric parameters like impeller shape, size, and baffles of the vessel need to be reconfigured to increase the power input.
- The nanofluids do not affect the power dissipation characteristics of the vessel. While nanofluids improve the vessel's heat transfer characteristics for user applications, their high cost does not make economic sense.
- The temperature rise of the fluid in the vessel due to viscous dissipation depends on the

specific heat of the base fluid. The vessel can be optimized for energy storage by using high specific heat fluid like water, or it can be optimized for high-temperature rise by using low specific heat fluid-like EG.

5.2 Recommendations

There are many ways in which the heat generator can be improved and implemented as a commercial device. A few of the recommendations are noted below:

- The impeller and vessel designs need to be such that cavitation is avoided. This can be achieved by either limiting the high rotational speed or modifying the impeller.
- While the device is efficient at energy conversion, its stand-alone performance is limited. The heat generator can be used as a pre-heater for an electric water heater to improve the heating process's overall efficiency.
- CFD could be used to model the viscous dissipation and the performance of the heat generator can be investigated numerically.
- A self-starting wind turbine can be developed which could power this heat generator.

References

[1] T. Wang, "Consumption of electricity worldwide from 1980 to 2016," Statista, 2019. [Online]. Available: https://www.statista.com/statistics/280704/world-power-consumption/.

[2] Xi Lu, Michael B. McElroy, and Juha Kiviluoma, "Global potential for wind-generated electricity," *Proceedings of the National Academy of Sciences,* vol. 106, no. 27, pp. 10933-10938, 2009.

[3] S. Canada, "Households and the Environment Survey," 2011.

[4] J. P. Joule, "On the mechanical equivalent of heat, as determined by the heat evolved by the friction of fluids," *Philosophical Magazine Series,* vol. 3, pp. 173-176, 1847.

[5] Christopher Barrington-Leigh, Mark Ouliaris, "The renewable energy landscape in Canada: A spatial analysis," *Renewable and Sustainable Energy Reviews,* vol. 75, 2017.

[6] S. B. Pope, Turbulent Flows, Cambridge University Press, 2012.

[7] L. W. B. Browne, R. A. Antonia, D. A. Shah, "Turbulent energy dissipation in a wake," *J. Fluid Mech.,* vol. 179, pp. 307-326, 1987.

[8] S. C. S. Tavoularis, " Experiments in nearly homogeneous turbulent shear flow with a uniform mean temperature gradient. Part 1," *J. Fluid Mech.,* vol. 104, pp. 311-347, 1981.

[9] C. J. Lawn, "The determination of the rate of dissipation in turbulent pipe flow.," *J . Fluid Mech.,* vol. 48, pp. 477-505, 1971.

[10] H. F. I. Wygnanski, "Some measurements in the self-preserving jet.," *J . Fluid Mech,* vol.

38, pp. 577-612, 1969.

[11] I. W. E. GUTMARK, "The planar turbulent jet.," *J. Fluid Mech. ,* vol. 73, pp. 465-495, 1976.

[12] J. Laufer, "The structure of turbulence in fully developed pipe flow.," NACA Report 1174, 1954.

[13] L. F. Richardson, Weather Prediction by Numerical Process, Cambridge: Cambridge University Press, 1922.

[14] A. N. Kolmogorov, "The local structure of turbulence in incompressible viscous fluid for very large Reynolds numbers.," *Dokl. Akad. Nauk SSSR,* vol. 30, pp. 299-303, 1941.

[15] Y. V. Roustiam Chakirov, "Direct Conversion of Wind Energy into Heat Using Joule Machine," *International Conference on Environmental and Computer Science ,* vol. 19, 2011.

[16] M. Katawaluwa, H. Zhang, Y. Vagapov and J. Evans, "Simulation of Wind Heat Generator," in *IEEE International Conference on Electro/Information Technology*, East Lansing, MI, 2006.

[17] H. T. Yasuhito Nakatake, "A new maritime lifesaving distiller driven by wind," *Desalination,* vol. 177, pp. 31-42, 2005.

[18] Kang YANG, Xian-Peng SUN1, Yu GUO, Sheng-Shan BI and Xin-Yang QIU, "Experimental Study on the Performance of Wind Stirring System with different working fluids," in *International Conference on Energy Development and Environmental Protection*, 2018.

[19] N.C. Panja, D.P. Rao, "Power input measurement from temperature rise data in mechanically agitated contractors," *Institution of Chemical Engineers,* pp. 24-27, 1992.

[20] Mr. Syed Mohammed Tahmid, Mr. Bilal Saleh Gill, Dr. Kee M Park, Yeong Ryu, and Prof. SangHoon Lee, "Optimization and testing of a first generation cavitation heat pump," in *ASEE Annual Conference & Exposition*, Atlanta, Georgia, 2013.

[21] Eastman, Stephen U. S. Choi and J. A., "Enhancing Thermal Conductivity of Fluids with Nanoparticles," Energy Technology Division and Materials Science Division Argonne National Laboratory, Argonne, IL 60439, 1995.

[22] Y. Li, J. Zhou, S. Tung, E. Schneider, and S. Xi, "A review on development of nanofluid preparation and characterization," *Powder Technology,* vol. 196, no. 2, pp. 89-101, 2009.

[23] Mohamoud Jama, Tejvir Singh, Seifelislam Mahmoud Gamaleldin, Muammer Koc, Ayman Samara, Rima J. Isaifan, and Muataz A. Atieh, "Critical Review on nanofluids: Preperation, Characterization, and Applications," *Journal of Nanomaterials,* vol. 2016, 2016.

[24] Cho, B. C. Pak and Y. I., "Hydrodynamic and heat transfer study of dispersed fluids with submicron metallic oxide particles," *Experimental Heat Transfer,* vol. 11, no. 2, pp. 151-170, 1998.

[25] M. Saeedinia, M. A. Akhavan-Behabadi, and P. Razi, "Thermal and rheological characteristics of CuO-Base oil nanofluid flow inside a circular tube," *International Communications in Heat and Mass Transfer,* vol. 39, no. 1, pp. 152-159, 2012.

[26] C.J. Ho, W.K. Liu, Y.S. Chang, C.C. Lin, "Natural convection heat transfer of alumina-

water nanofluid in vertical square enclosures: An experimental study," *International Journal of Thermal Sciences,* vol. 49, pp. 1345-1353, 2010.

[27] Das, R. Vajjha and D., "Measurements of specific heat and density of Al2O3 nanofluid," in *Proceedings of the Mesoscopic, Nanoscopic and Macroscopic Materials: Proceedings of the International Workshop on Mesoscopic, Nanoscopic and Macroscopic Materials*, Bhubaneswar, India, 2008.

[28] I. M. Mahbubul, R. Saidur, and M. A. Amalina, "Thermal conductivity, viscosity and density of R141b refrigerant based nanofluid," *Procedia Engineering,* vol. 56, pp. 310-315, 2013.

[29] A. Einstein, "Eine neue Bestimmung der Molekuldimensionen," *Annalen der Physik,* vol. 324, no. 2, pp. 289-306, 1906.

[30] H. C. Brinkman, "The viscosity of concentrated suspensions and solutions.," *The Journal of Chemical Physics,* vol. 20, no. 4, p. 571, 1952.

[31] G. K. Batchelor, "The effect of Brownian motion on the bulk stress in a suspension of spherical particles," *Journal of Fluid Mechanics,* vol. 83, no. 1, pp. 97-117, 1977.

[32] M. M. Heyhat, F. Kowsary, A. M. Rashidi, S. Alem Varzane Esfehani, and A. Amrollahi, "Experimental investigation of turbulent flow and convective heat transfer characteristics of alumina water nanofluids in fully developed flow regime,," *International Communications in Heat and Mass Transfer,* vol. 39, no. 8, pp. 1272-1278, 2012.

[33] A. Zamzamian, S. N. Oskouie, A. Doosthoseini, A. Joneidi, and M. Pazouki, "Experimental investigation of forced convective heat transfer coefficient in nanofluids of

Al2O3/EG and CuO/ EG in a double pipe and plate heat exchangers under turbulent flow," *Experimental Thermal and Fluid Science,* vol. 35, no. 3, pp. 495-502, 2011.

[34] Q. L. a. Y. Xuan, "Convective heat transfer and flow characteristics of Cu-water nanofluid," *Science in China Series E: Technolgical Science,* vol. 45, no. 4, pp. 408-416, 2002.

[35] Y. X. a. Q. Li, "Investigation on convective heat transfer and flow features of nanofluids," *Journal of Heat Transfer,* vol. 125, no. 1, pp. 151-155, 2003.

[36] J. Albadr, S. Tayal, and M. Alasadi, "Heat transfer through heat exchanger using Al2O3 nanofluid at different concentrations," *Case Studies in Thermal Engineering,* vol. 1, no. 1, pp. 38-44, 2013.

[37] X. Wang, X. Xu, and S. U. S. Choi, "Thermal conductivity of nanoparticle—fluid mixture,," *Journal of Thermophysics and Heat Transfer,* vol. 13, no. 4, pp. 474-480, 1999.

[38] A. T. Utomo, H. Poth, P. T. Robbins, and A. W. Pacek, "Experimental and theoretical studies of thermal conductivity, viscosity and heat transfer coefficient of titania and alumina nanofluids," *International Journal of Heat and Mass Transfer,* vol. 55, no. 25-26, pp. 7772-7781, 2012.

[39] S. W. Lee, S. D. Park, S. Kang, I. C. Bang, and J. H. Kim, "Investigation of visocity and thermal conductivity of SiC nanofluids for heat transfer applications.," *International Journal of Heat and Mass Transfer,* vol. 54, no. 1-3, pp. 433-438, 2011.

[40] Y. Ding, H. Alias, D. Wen, and R. A. Williams, "Heat transfer of aqueous suspensions of carbon nanotubes (CNT nanofluids)," *International Journal of Heat and Mass Transfer,*

vol. 49, no. 1-2, pp. 240-250, 2006.

[41] P. K. Namburu, D. P. Kulkarni, D. Misra, and D. K. Das, "Viscosity of copper oxide nanoparticles dispersed in ethylene glycol and water mixture," *Experimental Thermal and Fluid Science,* vol. 32, no. 2, pp. 397-402, 2007.

[42] C. T. Nguyen, F. Desgranges, N. Galanis et al., "Viscosity data for Al2O3-water nanofluid—hysteresis: is heat transfer enhancement using nanofluids reliable?," *International Journal of Thermal Science,* vol. 47, no. 2, pp. 103-111, 2008.

[43] D. P. Kulkarni, D. K. Das, and R. S. Vajjha, "Application of nanofluids in heating buildings and reducing pollution," *Applied Energy,* vol. 86, no. 12, pp. 2566-2573, 2009.

[44] J. Garg, B. Poudel, M. Chiesa, et. al, "Enhanced thermal conductivity and viscosity of copper nanoparticles in ethylene glycol nanofluid," *JOURNAL OF APPLIED PHYSICS,* vol. 103, 2008.

[45] Yurong He, Yi Jin , Haisheng Chen , Yulong Ding , Daqiang Cang , Huilin Lu, "Heat transfer and flow behaviour of aqueous suspensions of TiO2 nanoparticles (nanofluids) flowing upward through a vertical pipe," *International Journal of Heat and Mass Transfer,* vol. 50, pp. 2272-2281, 2007.

[46] S.W. Lee, S.D. Park, S. Kang, I.C. Bang, J.H. Kim, "Investigation of viscosity and thermal conductivity of SiC nanofluids for heat transfer applications," *International Journal of Heat and Mass Transfer,* vol. 54, pp. 433-438, 2011.

[47] R. Prasher, D. Song, J. Wang, P. Phelan, "Measurements of nanofluid viscosity and its implications for thermal applications,," *Applied Physics Letters,* vol. 89, 2006.

[48] H. Chen, S. Witharana, Y. Jin, C. Kim, Y. Ding, "Predicting thermal conductivity of liquid suspensions of nanoparticles (nanofluids) based on rheology," *Particuology,* vol. 7, pp. 151-157, 2009.

[49] H. Zhu, C. Li, D. Wu, C. Zhang, Y. Yin, "Preparation characterization viscosity and thermal conductivity of CaCO3 aqueous nanofluids," *Sci. China Technol. Sci,* vol. 2, pp. 360-368, 2010.

[50] K.B. Anoop, S. Kabelac, T. Sundararajan, S.K. Das, "Rheological and flow characteristics of nanofluids: influence of electroviscous effects and particle agglomeration," *Journal of Applied Physics,* vol. 106, 2009.

[51] O. T. F. A. J. Chevalier, "Rheological properties of nanofluids flowing through microchannels," *Appl. Phys. Lett. ,* vol. 91, pp. 2272-2281, 2007.

[52] T. D. Madhusree Kole, "Viscosity of alumina nanoparticles dispersed in car engine coolant," *Experimental Thermal and Fluid Science,* vol. 34, pp. 677-683, 2010.

[53] Y. X, W. Roetzel, "Conceptions for heat transfer correlation of nanofluids," *International Journal of Heat and Mass Transfer,* vol. 43, no. 19, pp. 3701-3707, 2000.

[54] S. Z. a. R. Ni, "Measurement of the specific heat capacity of water-based Al2O3 nanofluid," *Applied Physics Letter,* vol. 92, no. 9, 2008.

[55] D. K. D. a. D. R. J. R. Satti, "Specific heat measurements of five different propylene glycol based nanofluids and development of a new correlation," *International Journal of Heat and Mass Transfer,* vol. 94, pp. 343-353, 2016.

[56] De Robertis, E., Cosme, E. H. H., Neves, R. S., Kuznetsov, A. Y., Campos, A. P. C.,

Landi, S. M., & Achete, C. A., "Application of the modulated temperature differential scanning calorimetry technique for the determination of the specific heat of copper nanofluids," *Applied Thermal Engineering,* vol. 41, pp. 10-17, 2012.

[57] J. C. Maxwell, A Treatise on Electricity and Magnetism, Clarendon, Oxford, UK: 1873, 1873.

[58] D. A. Bruggeman, "Berechnung verschiedener physikalischer Konstanten von heterogenen Substanzen. I. Dielektrizitätskonstanten und Leitfähigkeiten der Mischkörper aus isotropen Substanzen," *Annalen der Physik,* vol. 416, no. 7, pp. 636-664, 1935.

[59] Crosser, R. L. Hamilton and O. K., "Thermal conductivity of heterogeneous two-component systems," *Industrial & Engineering Chemistry Fundamentals,* vol. 1, no. 3, pp. 187-191, 1962.

[60] S. S. O. M. &. S. W. Mohammad Hemmat Esfe, "Thermal conductivity of Al2O3/water nanofluids," *Journal of Thermal Analysis and Calorimetry,* vol. 117, pp. 675-681, 2014.

[61] K.B. Anoop, T. Sundararajan, Sarit K. Das, "Effect of particle size on the convective heat transfer in nanofluid in the developing region," *International Journal of Heat and Mass Transfer,* vol. 52, pp. 2189-2195, 2009.

[62] C. H. L. a. G. P. Peterson, "Experimental investigation of temperature and volume fraction variations on the effective thermal conductivity of nanoparticle suspensions (nanofluids)," *Journal of Applied Physics,* vol. 99, 2006.

[63] I. US Research Nanomaterials. [Online]. Available: https://www.us-nano.com/nanopowders.

[64] I. US Research Nanaomaterials. [Online]. Available: https://www.us-nano.com/dispersions.

[65] G. Zhou, Characteristics of Turbulence Energy Dissipation and Liquid-Liquid Dispersions in An Agitated Tank., Edmonton, Alberta: University of Alberta, 1997.

[66] J. B. G. Vincent W. Uhl, Mixing: Theory and Practice, Vol 1, New York and London: Academic Press, 1966.

[67] I. -. Wikipedia, Wikipedia, 2020. [Online]. Available: https://en.wikipedia.org/wiki/Impeller.

[68] J. C. Yungus A. Cengel, Fluid Mechanics: Fundamentals and Applications, Tata McGraw Hill Education Private, 2010.

[69] R. L. Bates, P. L. Fondy, and R. R. Corpstein, "Examination of Some Geometric Parameters of Impeller Power," *Ind. Eng. Chem. Process Des. Dev,,* vol. 2, no. 4, pp. 310-314, 1963.

[70] P. M. Doran, Bioprocess Engineering Principles, Academic Press, 2012.

[71] S. Aiba, "Flow patterns of liquids in agitated vessels.," *AIChE J.,* vol. 4, pp. 485-489, 1958.

[72] S. Nagata, K. Yamamoto, K. Hashimato, "Flow patterns of liquids in acylindrical mixing vessel with baffles.," *Mem. Fac. Eng, Kyoto University,* vol. 21, p. 260, 1959.

[73] R. L. Bates, P. L. Fondy, and R. R. Corpstein, "Examination of Some Geometric Parameters of Impeller Power," *ndustrial & Engineering Chemistry Process Design and Development ,* vol. 2, no. 4, pp. 310-314, 1963.

[74] Nagata, S., Yokoyama, T., and Maeda, H., *Mem. Fac. Eng., Kyoto Univ,* vol. 18, no. 13, 1956.

[75] Reflectix, [Online]. Available: https://www.reflectixinc.com/products/double-reflective-insulation/.

[76] L. London, "MDE Semiconductors Inc.," [Online]. Available: http://www.mdesemiconductor.com/what-is-a-thyristor-types-of-thyristors-and-their-uses/.

[77] [Online]. Available: https://www.mcmaster.com/7729K13/.

[78] "National Instruments.," [Online]. Available: https://www.ni.com/en-ca/support/model.cdaq-9178.html.

[79] "National Instruments," [Online]. Available: https://www.ni.com/en-ca/support/model.ni-9211.html.

[80] "National Instruments.," [Online]. Available: http://www.ni.com/en-us/support/model.ni-9237.html.

[81] Mettler Toledo, [Online]. Available: https://www.mt.com/ca/en/home/perm-lp/product-organizations/ana/TA-Cp_specific_heat_capacity.html.

[82] R. J. Moffat, "Describing the Uncertainties in Experimental Results," *Experimental Thermal and Fluid Science,* vol. 1, pp. 3-17, 1988.

[83] Jian Qu, Hui-ying Wu , Ping Cheng, "Thermal performance of an oscillating heat pipe with Al2O3–water nanofluids," *International Communications in Heat and Mass Transfer,* vol. 37, pp. 111-115, 2010.

[84] S. S. A. C. B. M. Chandrasekar, "Experimental investigations and theoretical determination of thermal conductivity and viscosity of Al2O3/water nanofluid," *Experimental Thermal and Fluid Science,* vol. 34, pp. 210-216, 2010.

[85] S. Suresh, P. Selvakumar, M. Chandrasekar, and V. S. Raman, "Experimental studies on heat transfer and friction factor characteristics of Al2O3/water nanofluid under turbulent flow with spiraled rod inserts," *Chemical Engineering and Processing: Process Intensification,* vol. 53, pp. 24-30, 2012.

[86] S. Soltani, S. Etemad, J. Thibault, "Pool boiling heat transfer of non-Newtonian nanofluids," *International Communications in Heat and Mass Transfer,* vol. 37, pp. 29-33, 2010.

[87] Yi-Hsuan Hung, Tun-Ping Teng, Bo-Gu Lin, "Evaluation of the thermal performance of a heat pipe using alumina nanofluids," *Experimental Thermal and Fluid Science,* vol. 44, pp. 504-511, 2013.

[88] Lee, S., Choi, S. U.-S., Li, S., & Eastman, J. A., "Measuring Thermal Conductivity of Fluids Containing Oxide Nanoparticles," *Journal of Heat Transfer,* vol. 121, no. 2, pp. 280-289, 1999.

[89] Wozniak, M., Danelska, A., Kata, D., & Szafran, M., "New anhydrous aluminum nitride dispersions as potential heat-transferring media.," *Powder Technology,* vol. 235, pp. 717-722, 2013.

[90] W.H. Azmi, K.V. Sharma, P.K. Sarma, Rizalman Mamat, , Shahrani Anuar, V. Dharma Rao, "Experimental determination of turbulent forced convection heat transfer and friction

factor with SiO2 nanofluid," *Experimental Thermal and Fluid Science,* vol. 53, pp. 103-111, 2013.

[91] "Aluminum Oxide Nanopowder / Nanoparticles (Al2O3, gamma, 99.99%, 5nm, Hydrophilic)," US Research Nanomaterials, Inc, [Online]. Available: https://www.us-nano.com/inc/sdetail/13036.

[92] SKF Reliability Systems, "Vibration Diagnostic Guide".

[93] H. P, "Evaluation, neuentwicklung und optimierung des eigenschaftsprofils von salzschmelzen für die verwendung als wärmeträgerfluide.," *PhD thesis. Bergische Universität, Wuppertal,* 2013.

[94] Lasfargues M, Geng Q, Cao H, Ding Y, "Mechanical dispersion of nanoparticles and its effect on the specific heat capacity of impure binary nitrate salt mixtures.," *Nanomaterials,* vol. 5, pp. 1136-1146, 2015.

[95] "Online calculator, figures and tables showing specific heat of liquid water at constant volume or constant pressure at temperatures from 0 to 360 °C (32-700 °F) - SI and Imperial units," The Engineering Toolbox, [Online]. Available: https://www.engineeringtoolbox.com/specific-heat-capacity-water-d_660.html.

[96] I.B., Rabinovich,P.N, Nikolaev, "The Isotope Effect in the Heat Capacity of certain Deuterated Compounds," *Dokl.Akad.Nauk SSSR,* vol. 142 , pp. 1335-1338, 1962.

[97] N., Manohara Murthy, S.V., Subrahmanyam, "Behaviour of Excess Heat Capacity of Aqueous Non-Electrolytes.," *Indian J.Pure Appl.Phys,* pp. 485-489, 1977.

[98] M.I., Paz Andrade, E., Recacho, J.M., Paz Fernandez, "Determinacion de calores

especificos de liquidos.," *Acta Cient.Compostelana 5,* pp. 49-55, 1968.

[99] G.Kh., Mukhamedzyanov, Z.I., Zaripov., " Wärmekapazität von Polyetylenglykolen und ihren Mischungen.," *Oniitekhim ,* pp. 1-8, 1988.

[100] S. Watanabe, A. Furukawa, Y. Yoshida, "Theoretical Analysis of Thermodynamic Effect of Cavitation in Cryogenic Inducer Using Singularity Method," *International Journal of Rotating Machinery,* vol. 2008, 2008.

[101] D. R. Lide, CRC Handbook of Chemistry and Physics, CRC Press, 2004, pp. 6-8.

[102] "Temperature Dependent Properties. [PVP] Vapor pressure of ETHYLENE GLYCOL," Chemical Engineering Research Information Center, [Online]. Available: https://www.cheric.org/research/kdb/hcprop/showcoef.php?cmpid=909&prop=PVP.

[103] "Energy Hub," [Online]. Available: https://www.energyhub.org/electricity-prices/#:~:text=Average%20Electricity%20Prices,if%20you%20exclude%20the%20territories.

[104] E. U. Sub-Group:, "Efficiency in Electricity Generation," Union of the Electricity Industry - EURELECTRIC , July 2003.

Appendix I: Engineering Drawings

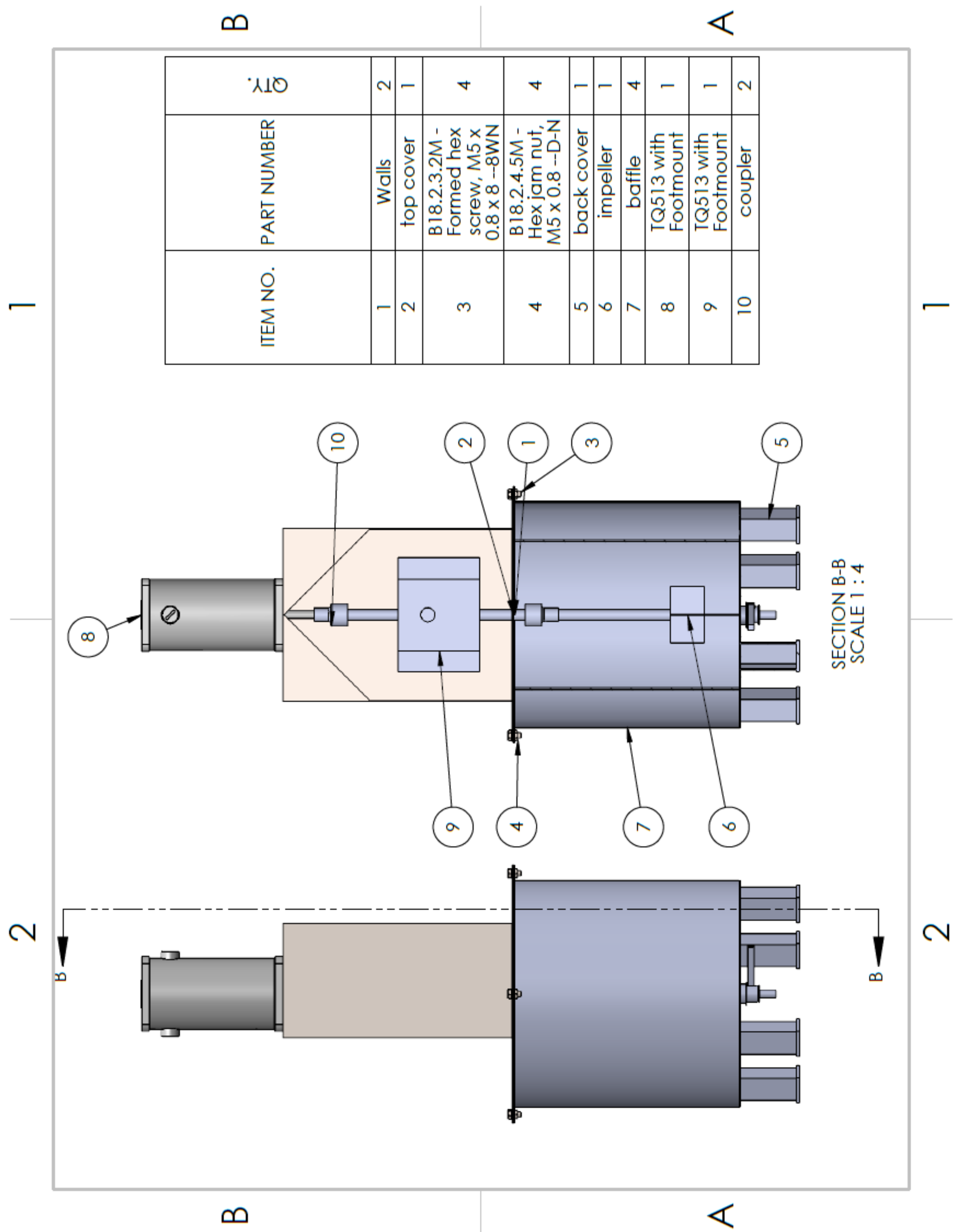

ITEM NO.	PART NUMBER	QTY.
1	Walls	2
2	top cover	1
3	B18.2.3.2M - Formed hex screw, M5 x 0.8 x 8 --8WN	4
4	B18.2.4.5M - Hex jam nut, M5 x 0.8 --D-N	4
5	back cover	1
6	impeller	1
7	baffle	4
8	TQ513 with Footmount	1
9	TQ513 with Footmount	1
10	coupler	2

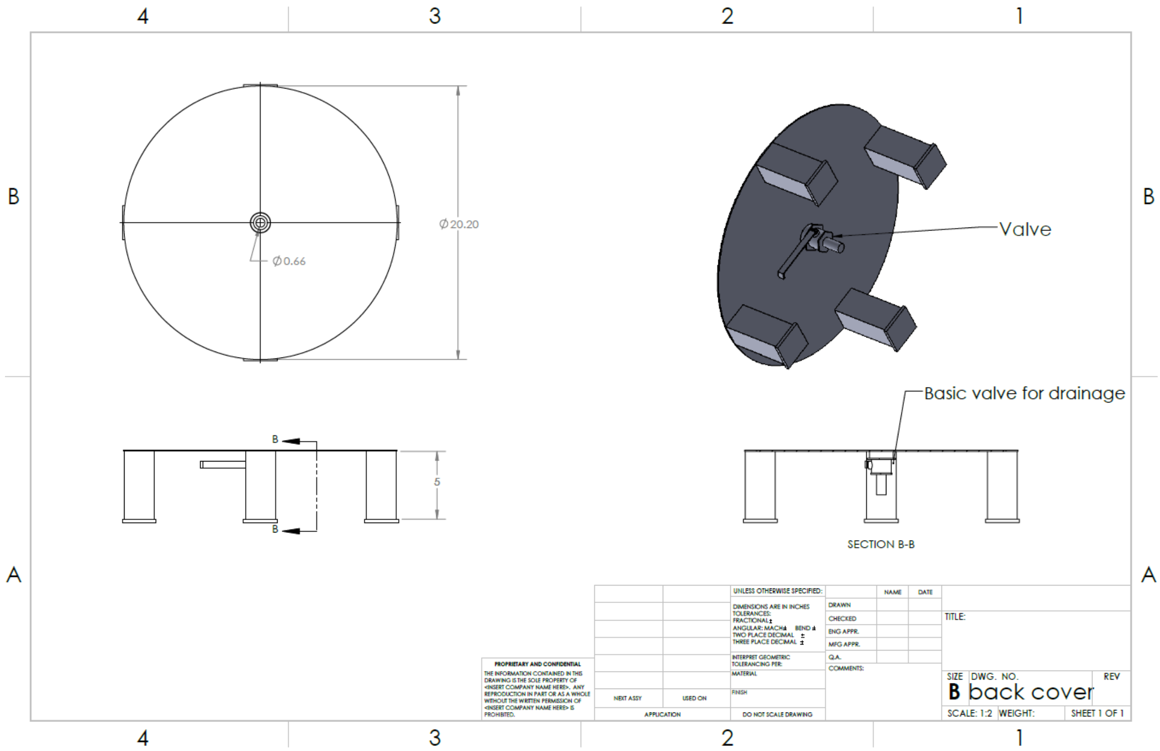

Ø20.20
Ø0.66
Valve
Basic valve for drainage
5
SECTION B-B
UNLESS OTHERWISE SPECIFIED:
PROPRIETARY AND CONFIDENTIAL
TITLE:
SIZE DWG. NO. REV
B back cover
SCALE: 1:2 WEIGHT: SHEET 1 OF 1

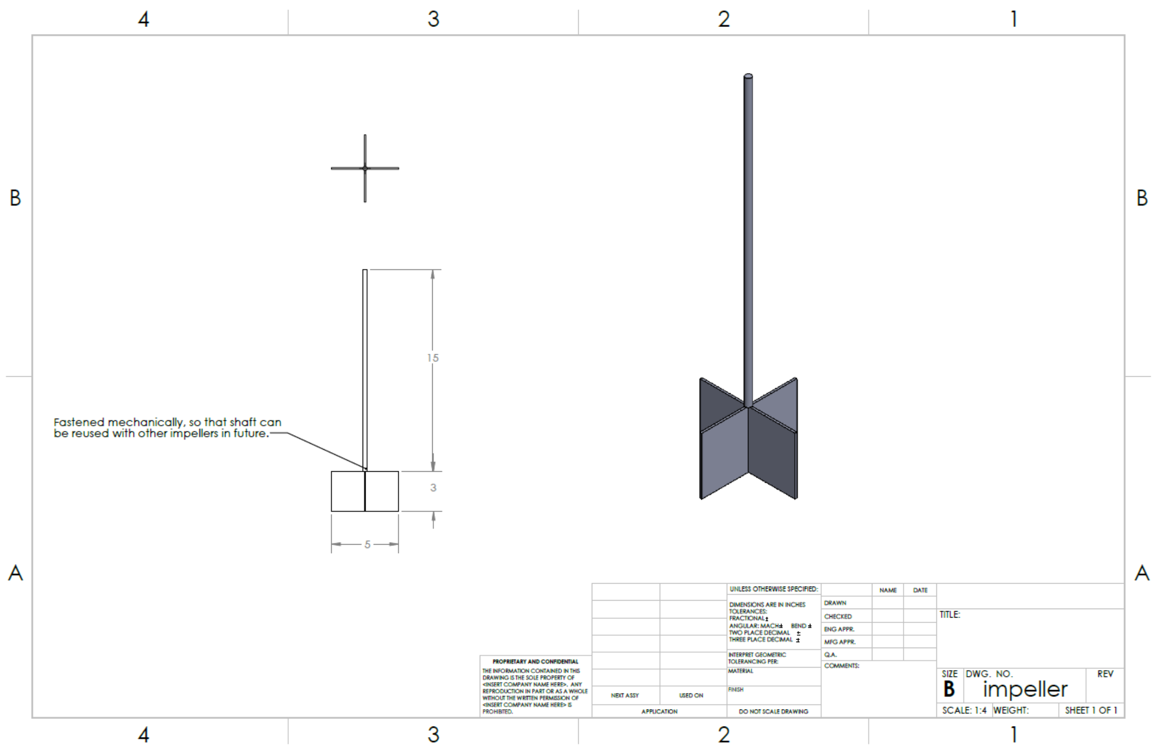

Fastened mechanically, so that shaft can be reused with other impellers in future.
15
3
5
UNLESS OTHERWISE SPECIFIED:
PROPRIETARY AND CONFIDENTIAL
TITLE:
SIZE DWG. NO. REV
B impeller
SCALE: 1:4 WEIGHT: SHEET 1 OF 1

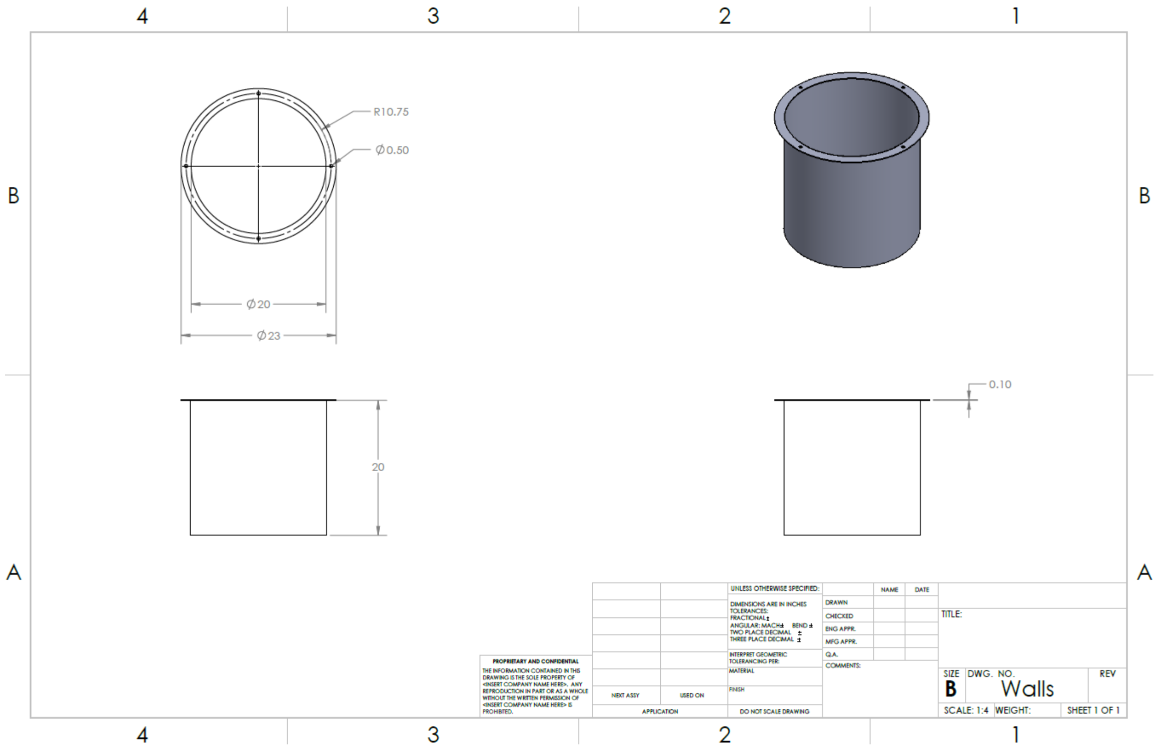
R10.75
Ø0.50
Ø20
Ø23
20
0.10
TITLE:
Walls
SIZE B
DWG. NO.
REV
SCALE: 1:4
WEIGHT:
SHEET 1 OF 1
UNLESS OTHERWISE SPECIFIED:
PROPRIETARY AND CONFIDENTIAL
DO NOT SCALE DRAWING

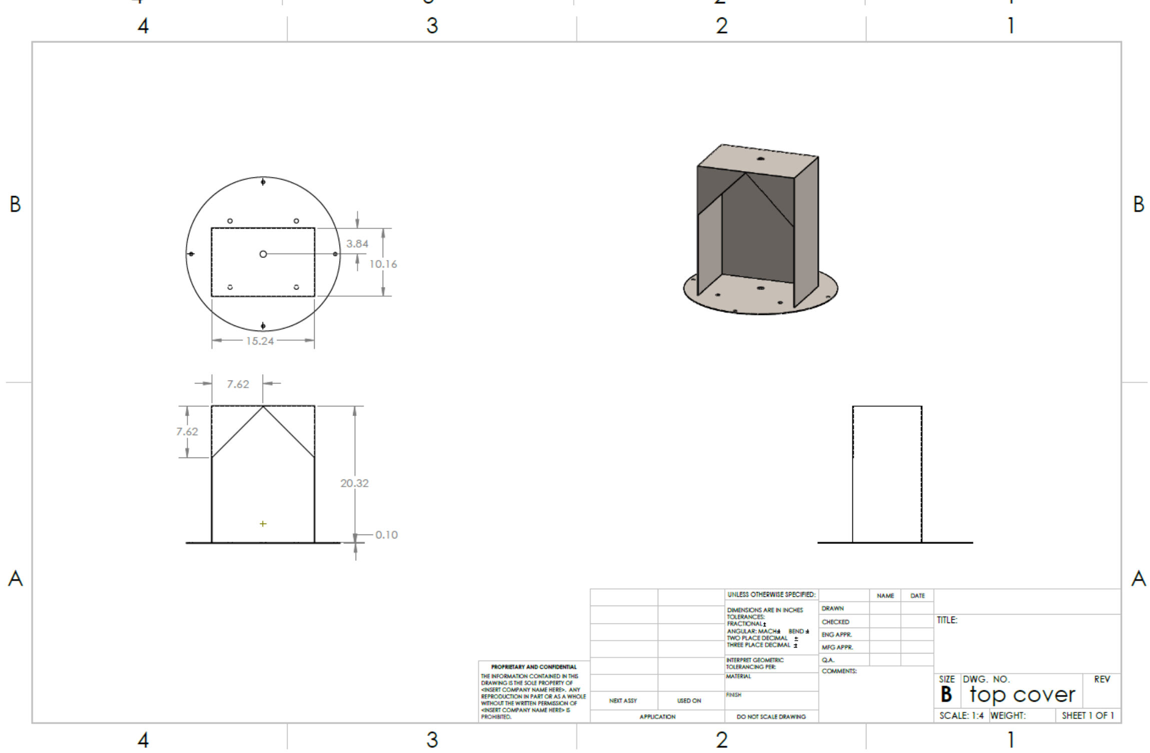
3.84
10.16
15.24
7.62
7.62
20.32
0.10
TITLE:
top cover
SIZE B
DWG. NO.
REV
SCALE: 1:4
WEIGHT:
SHEET 1 OF 1
UNLESS OTHERWISE SPECIFIED:
PROPRIETARY AND CONFIDENTIAL
DO NOT SCALE DRAWING

Appendix II: Example of Uncertainty Analysis

The efficiency of energy conversion from kinetic to sensible heat is defined as:

$$\eta = \frac{mc_p \Delta T}{\tau \cdot \omega_{cyc}}$$

The uncertainty is defined as:

$$\frac{\delta\eta}{\eta} = \left\{ \left(\frac{\delta m}{m}\right)^2 + \left(\frac{\delta c_p}{c_p}\right)^2 + \left(\frac{\delta \Delta T}{\Delta T}\right)^2 + \left(\frac{\delta\tau}{\tau}\right)^2 + \left(\frac{\delta\omega_{cyc}}{\omega_{cyc}}\right)^2 \right\}^{\frac{1}{2}}$$

The maximum uncertainty.

$$\frac{\delta\eta}{0.9912} = \left\{ \left(\frac{1}{5057}\right)^2 + \left(\frac{0.15}{4.3}\right)^2 + \left(\frac{0.5}{1.99}\right)^2 + \left(\frac{0.2}{1.4261}\right)^2 + \left(\frac{0.5}{756}\right)^2 \right\}^{\frac{1}{2}}$$

$$\delta\eta = 0.2873$$

The bias error is ignored from the calculations as its presence will not have a measurable effect on the final number.